Arabian Journal of Geosciences (2022) 15: 983
https://doi.org/10.1007/s12517-022-10252-w

ORIGINAL PAPER

Geochronology, geochemical characteristics, and geological implications of the Guangnan pluton in the Middle Segment of the Zhuguangshan batholith, South China

Sumei Zhang[1,2] · Yang Wang[3] · Junbin Zhu[1] · Tianjing Jing[4] · Xiaohan Wang[2]

Received: 24 November 2021 / Accepted: 29 April 2022 / Published online: 12 May 2022

Abstract
The Guangnan pluton is located on the central of South China and the junction of Hunan and Jiangxi provinces. The zircon U–Pb age dating results show that the pluton formed between 164 and 148 Ma. The pluton composed of biotite granite, two-mica granite, and garnet-bearing granite, which contain higher SiO_2 (72.82–76.16wt.%), lower Zr (83.5–118 μg/g), and ASI > 1. These geochemical characteristics are very similar to high-silicon peraluminous light-colored granite or ferroan calc-alkaline high-silica granite, or muscovite-containing peraluminous granite (MPG) type. The zircon $\varepsilon_{Hf}(t)$ value (−3.94–−11.67) and those of inherited zircon characteristics indicate that multiple melting of lower crustal materials, which were formed in the Caledonian, Indosinian, and Early Jurassic periods, acted as part of the source rock of the mid-late Jurassic Guangnan high-silica granite in the Zhuguangshan area. This study shows that the high-silica granite in Guangnan area is the production of the post-collision stage of the collision between Western Pacific ancient land and the South China orogenic belt in Early Yanshanian. In the "post-collision" stage during the Middle Jurassic, the magmatic material was formed by partially melting and multiple remelting of the lower crustal metamorphic argillaceous rock and/or metamorphic acidic igneous rock because of the heat from the base-invasion basic magma.

Keywords Geochronology · High-silica granite · Early Yanshanian · Guangnan pluton · Zhuguangshan batholith

Introduction

Since Neoproterozoic, multi-stage tectono-magmatic activities were reported in South China Craton (Ren et al. 2013). In South China, magmatic activities were most developed during Jurassic, and a variety of granitic magma intruded South China, including I-type, S-type, and A-type granites. With strong magmatic activity, a large number of non-ferrous metal deposits were formed. W-Sn deposits are the most typical deposits in the Nanling metallogenic belt (Mao et al. 2009, 2008; Chen et al. 2014; Shu et al. 2021; Sun 2018; Xia et al. 2021). The outcropping area of the Zhuguangshan batholith is more than 5000 km^2, it is exposed in the central part of the Nanling tectonic belt, and the batholith is composed of multiple Caledonian, Indosinian, and Yanshanian granitic plutons forming the Wanyangshan and Zhuguangshan at the boundary of Hunan, Jiangxi, and Guangdong (Zhou 2007). The Yanshanian period is an important metallogenic period, which consists of three stages of 150–160 Ma, 140–130 Ma, and 100–90 Ma (Mao et al. 2008; Fan et al. 2017). Minerals are developed in the southern part of the Zhuguangshan batholith, especially tungsten and tin minerals, and the research is detailed, while the northern part is relatively lacking due to the lack of minerals. Guangnan pluton is located in center east part of the Zhuguangshan batholith (Fig. 1). Researchers have little research on the Guangnan pluton; they mainly focused on the division of intrusive rock units and chronology (Zheng 1988; Li 1990;

Responsible Editor: Domenico M. Doronzo

✉ Yang Wang
wangyang@cugb.edu.cn

[1] Institute of Geology, Chinese Academy of Geological Sciences, Beijing 100037, China

[2] Hebei Key Laboratory of Strategic Critical Mineral Resources, College of Earth Science, Hebei GEO University, Shijiazhuang 050031, China

[3] School of Earth Sciences and Resources, China University of Geosciences, 100083 Beijing, China

[4] Huaxin College of Hebei GEO University, Shijiazhuang 050700, China

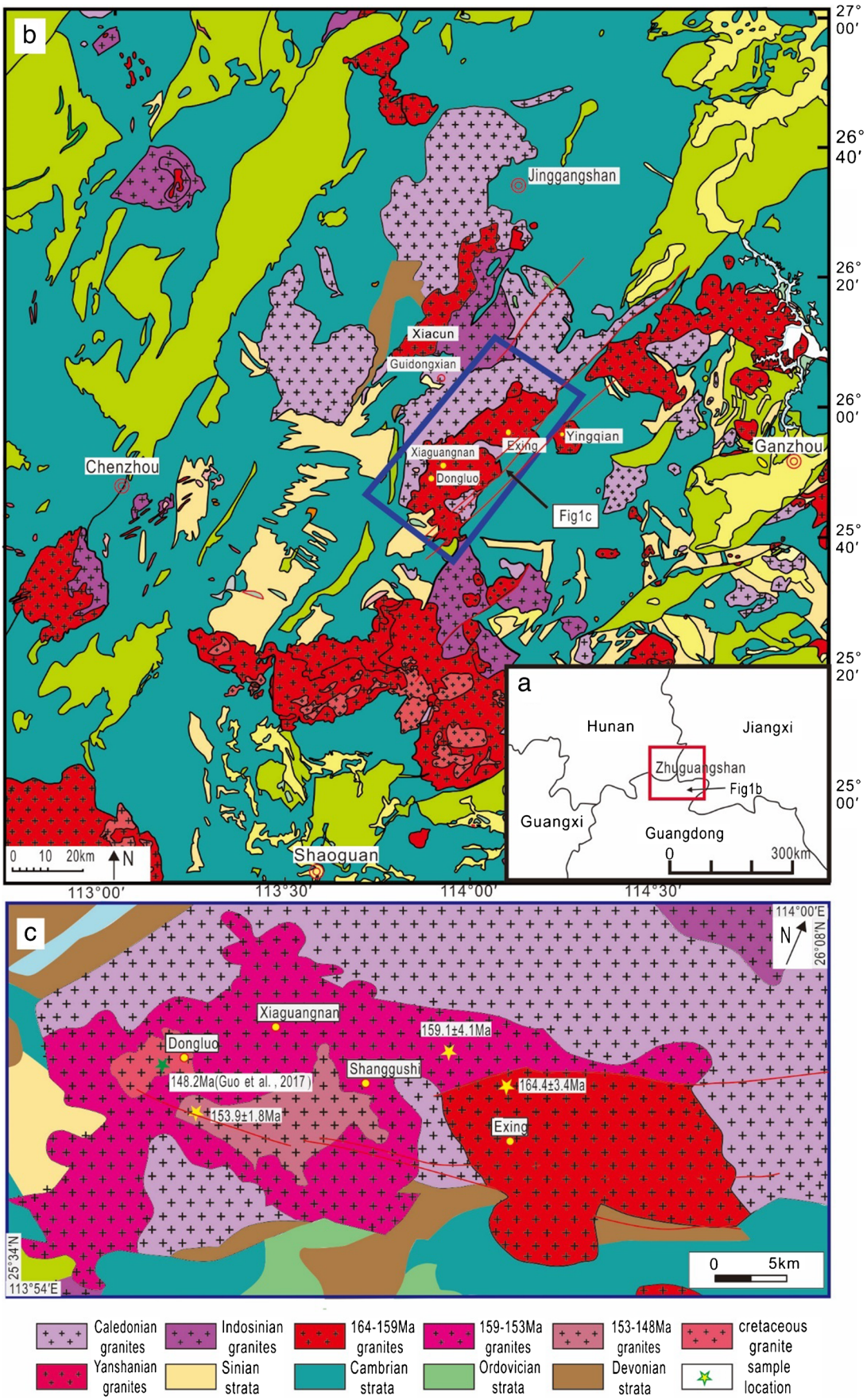
b
Jinggangshan
Xiacun
Guidongxian
Yingqian
Exing
Xiaguangnan
Dongluo
Chenzhou
Ganzhou
Fig1c
Shaoguan
0 10 20km N
27° 00′
26° 40′
26° 20′
26° 00′
25° 40′
25° 20′
25° 00′
113°00′
113°30′
114°00′
114°30′
a
Hunan
Jiangxi
Zhuguangshan
Fig1b
Guangxi
Guangdong
0 300km
c
114°00′E
26°08′N
N
Xiaguangnan
Dongluo
159.1±4.1Ma
Shanggushi
148.2Ma(Guo et al., 2017)
164.4±3.4Ma
153.9±1.8Ma
Exing
0 5km
25°34′N
113°54′E
Caledonian granites
Indosinian granites
164-159Ma granites
159-153Ma granites
153-148Ma granites
cretaceous granite
Yanshanian granites
Sinian strata
Cambrian strata
Ordovician strata
Devonian strata
sample location

◂**Fig. 1** Geological schematic diagram of Zhuguangshan (modified after 1: 500,000 scale geological and mineral map of the Nanling area (Hunan Geological Survey, 2002) and distribution map of granite in south China (Zhou 2007). The pluton in the dark blue area is the Guangnan pluton. The data of the green stars quoted from Guo et al. (2017), and the yellow stars is this paper

Guo et al. 2017). In this paper, we carried out comprehensive investigations and selected typical samples on field observation (Fig. 2), zircon laser ablation inductively coupled plasma mass spectrometry (LA-ICP-MS) U–Pb age dating, the characteristics of Hf isotopic, and whole-rock major and trace elements analysis, and combined with previous research results, to determine the formation age, geochemical characteristics, and geological significance of Guangnan pluton and provide conditions for the mineralogy in the northern part.

Geological background

During the Cambrian to Quaternary, the South China block has experienced the combined effect of multiple tectonic–magmatic cycles (Ren et al. 1990), including Caledonian cycle, Indosinian cycle, Yanshanian cycle, and the Himalayan cycle. During the Cambrian-Ordovician, the South China block was rifted, and the subsidence reached the strongest in the Early-Middle Ordovician, forming a huge thick marine sandy and muddy terrigenous clastic source clastic rock series with graptolite sheets and siliceous shale simultaneously. During the late Ordovician to early Silurian period, South China was involved in the Caledonian orogenic movement and developed large-scale granitic magmatic intrusions. The Caledonian orogenic movement led to the uplift of the South China fold and caused a regional angular unconformity between the Early Devonian or the later strata and the underlying strata, which including the Early Paleozoic or older strata. Then, the South China tectonic evolution entered the Post-Caledonian quasi-platform development stage (Ren and Li 2016). During the Indosinian, the basement of South China is influenced by the orogenic movement and caused the folds and fractures deformation, and accompanied by the syn-orogenic granitic magmatism simultaneously. On the Early Jurassic, South China was affected by local rifting and bimodal magmatic activity occurred in the region of southwestern Fujian-Southern to Jiangxi-Southern and Hunan (Chen et al. 1999; He et al. 2010). The sedimentary environment was generally transformed from marine facies to terrestrial facies in South China, except for the coast of Fujian and Guangdong. During middle Jurassic to the Early Cretaceous, the collision orogeny of the western Pacific ancient continent and the eastern margin of the Asian continent led to strong fold uplift and reverse faulting activities in South China, and large-scale granitic magma intrusions. At the same time, the materials of the Indosinian or earlier occurred extrusion folds, which were further strengthened, resulting in numerous reverse faults and related structures. During the Early Cretaceous, strike-slip and shear-extension deformations were developed and formed a series of faulted basins. Large-scale volcanic rocks developed in the Zhejiang-Fujian and Lower Yangtze regions, and A-type granite started to intrude at the coastal areas (Xing et al. 2008; Shu et al. 2009; Shu 2012; Liu et al. 2020). Since the Paleogene, the tectonic background of South China turned into the stage of extensional deformation. Because of the affection of the collision between the Philippine Sea plate and Taiwan, South China developed extrusion and deformation during the Neogene. Strong compression formed a reverse fault in the region and the red bed folded slightly, whereas the coast of Fujian and Guangdong and the continental shelf of the South China Sea continued to extend, rifts, with newly production of the basalt.

Nanling is the most developed Phanerozoic magmatism area in the South China orogenic belt. The granitic pluton at Nanling area is widely distributed and is characterized of multi-stage intrusion. It is also a mining area for rare and non-ferrous metals such as tungsten, tin, niobium, and tantalum (Zhou et al. 2006; Mao et al. 2009, 2008; Chen et al. 2014). The Zhuguangshan batholith, which is an important batholith that concentrated non-ferrous metal and uranium deposits in the Nanling magma-metallogenic belt, is located at the core of the South China orogenic belt. The southern half of the Zhuguangshan batholith (i.e., the southern body) outcropped in east–west direction, and exposed many Yanshanian plutons such as Jiufeng pluton, and also exposed the Caledonian and Indosinian plutons. The long axis direction of the northern half of the base (namely the northern body) outcropped in north–south direction, and the northern body is mainly composed of Caledonian and Indosinian intrusions, but Yanshanian granite plutons are less exposed compared to southern body.

Guangnan pluton is located at the junction of the Southern and the Northern bodies of the Zhuguangshan batholith, and extended into northeast in long axis under 2D view with an irregular shape pluton (Fig. 1). Its surrounding rocks are dominated by Caledonian granodiorite and biotite granite in the northwest and Sinian-Cambrian strata in the southwest, featuring superimposed fold structures in NE and NW direction. The southeast part of the pluton intruded into the Cambrian-Ordovician strata.

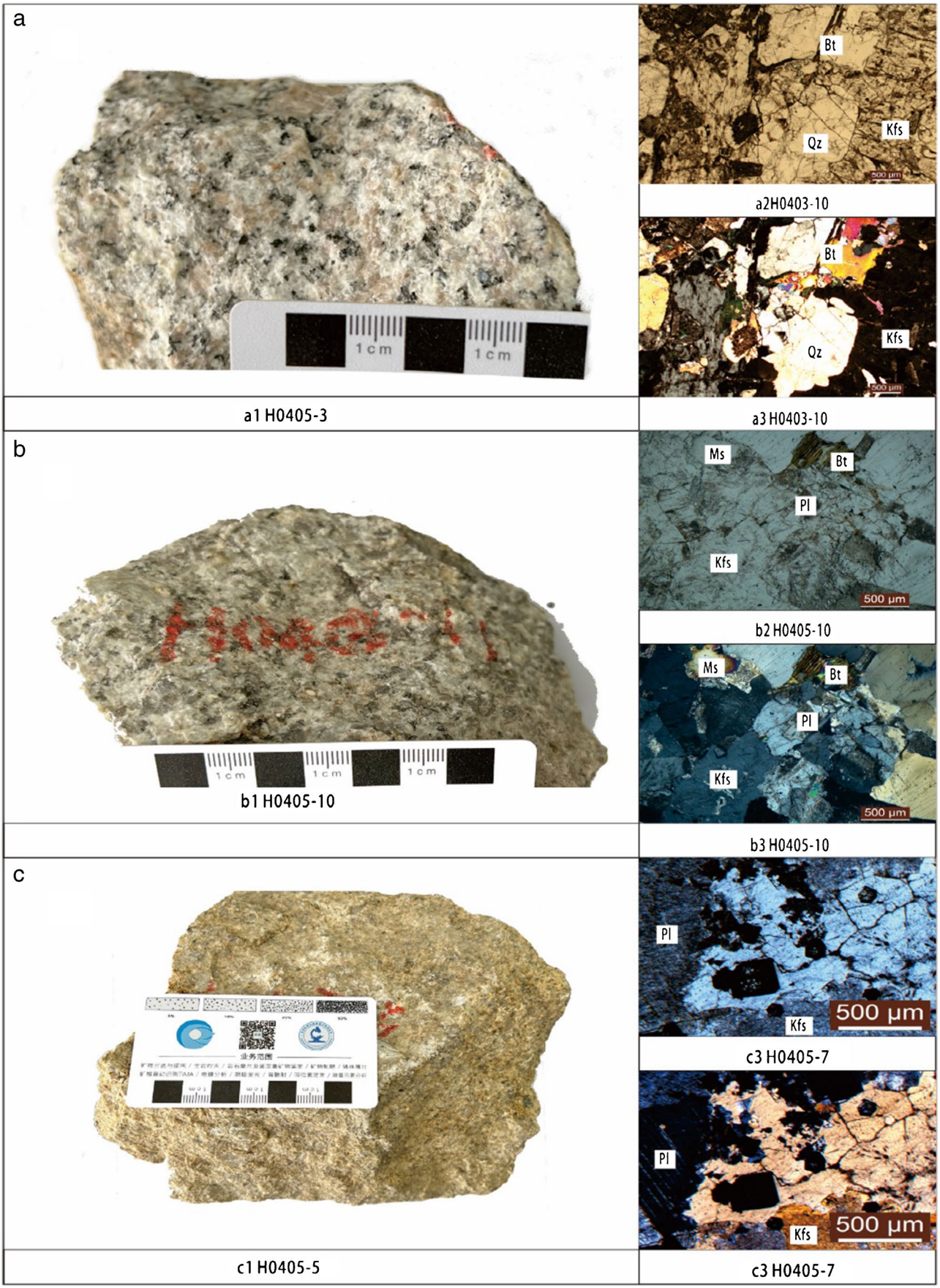
a
1 cm
1 cm
a1 H0405-3
Bt
Kfs
Qz
500 μm
a2H0403-10
Bt
Kfs
Qz
500 μm
a3 H0403-10
b
1 cm
1 cm
1 cm
b1 H0405-10
Ms
Bt
Pl
Kfs
500 μm
b2 H0405-10
Ms
Bt
Pl
Kfs
500 μm
b3 H0405-10
c
c1 H0405-5
Pl
Kfs
500 μm
c3 H0405-7
Pl
Kfs
500 μm
c3 H0405-7

◂**Fig. 2** The typical sample of Guangnan pluton. Figures (a), (b), and (c) are for biotite granite (H0405-3 and H0403-10), two-mica granite (H0405-10), and garnet biotite granite (H0405-7), respectively. Figures (a2), (b2), and (c2) are images of the biotite granite, two-mica granite, and garnet biotite granite under a single polarizer. Figures (a3), (b3), and (c3) are crossed polarizers, respectively

Petrography characteristics

Guangnan pluton is mainly composed of biotite granite, garnet biotite granite, and muscovite-bearing granite (Fig. 2).

Biotite granite (H0403-10) is of gray-white in color and porphyritic structure with medium coarse in sizes; these rocks are often weathered and loose in shape. The phenocrysts are mainly gray-white colorless K-feldspar (8%) with 2–4 cm in size, which can tell Castellin double crystal combined pattern clearly by naked eyes. The matrix minerals are 0.1–0.3 cm in size with medium- and fine-grained unequal grain structure and are mainly composed of quartz, biotite, K-feldspar, and plagioclase with accessory minerals including appatite, zircon, and spinel. The quartz (25% of the matrix) is anhedral in shape and 0.1–0.2 cm in size, and appears as quartz aggregation in some section. The biotite (10%) is dark in color and euhedral in shape with around 0.2–0.8 cm in size. The K-feldspar (40%) is euhedral plate in shape and 0.2–0.3 cm in size. The Plagioclase (15%) is euhedral off-white wide plate in shape and 0.2–0.3 cm in size.

Garnet biotite granite is of gray-white in color and porphyritic structure with medium fine in sizes. The phenocrysts of the rocks are mainly gray-white colorless K-feldspar (5–8%) with 0.2–0.8 cm in size. The matrix minerals are 0.01–0.02 cm in size with fine-grained structure and are mainly composed of quartz, biotite, K-feldspar, and plagioclase with accessory minerals including appetite, zircon, and spinel. The quartz (25%) of the matrix is anhedral in shape and 0.01 cm in size. The biotite (~5%) is dark brown in color and euhedral in shape with around 0.05 – 0.07 cm in size. The K-feldspar (~35%) is euhedral plate in shape and 0.2–0.3 cm in size. The plagioclase (~25%) is euhedral off-white wide plate in shape and 0.2–0.3 cm in size. The garnet (1 ~ 3%) is colorless with 0.02–0.08 cm in size.

Two-mica granite is of light red to gray-white in color and medium coarse in mineral sizes, porphyritic structure. The rocks weathered strongly in the field, and often loose in shape. The phenocrysts are mainly gray-white colorless K-feldspar (10%) and plagioclase (1–3%) with 2–4 cm in size, which can tell Castellin double crystal combined pattern clearly for K-feldspar and ring-shaped structure for plagioclase by naked eyes. The matrix minerals are 0.5–1.0 cm in size with coarse-grained unequal grain structure and are mainly composed of quartz, biotite, K-feldspar, and plagioclase with accessory minerals including appatite, zircon, and spinel. The quartz (30% of the matrix) is anhedral in shape and ~ 0.6–0.8 cm in size. The biotite (5–8%) is dark brown in color and euhedral in shape with around 0.6–0.8 cm in size. The muscovite (~ 1%) is colorless flake aggregates in shape with around 0.5–0.6 cm in size. The K-feldspar (30%) is euhedral plate in shape and 0.8–1.0 cm in size. The plagioclase (20%) is euhedral off-white wide plate in shape and 0.8–1.0 cm in size.

Sampling and analytical procedures

Zircon U–Pb dating, Lu–Hf isotope, and major and trace element compositions were conducted by LA-ICP-MS at Beijing Createch Testing Technology Co., Ltd.

Zircon U–Pb dating of the detailed operating conditions for the laser ablation system, the ICP-MS instrument, and data reduction are the same as described by Hou et al. (2009). Laser sampling was performed using a RESOlution 193 nm laser ablation system. The instrument used to acquire ion signal intensities was Analytik Jena PlasmaQuant MS Elite ICP-MS. Helium was applied as a carrier gas. Each analysis data acquisition from the sample incorporated a background acquisition of approximately 15–20 s (gas blank) followed by 45 s. Off-line raw data selection and integration of background and analyte signals and time drift correction and quantitative calibration for U–Pb dating were performed by ICPMSDataCal (Liu et al. 2010). Zircon GJ-1 was used as external standard for U–Pb dating, and was analyzed twice every 5 ~ 10 analyses. Time-dependent drifts of U-Th-Pb isotopic ratios were corrected using a linear interpolation (with time) for every 5–10 analyses according to the variations of GJ-1 (i.e., 2 zircon GJ-1 + 5–10 samples + 2 zircon GJ-1) (Liu et al. 2010). Uncertainty of preferred values for the external standard GJ-1 was propagated to the ultimate results of the samples. In all analyzed zircon grains, the common Pb correction was not necessary due to the low signal of common ^{204}Pb and high ^{206}Pb/^{204}Pb. U, Th, and Pb concentration was calibrated by NIST 610. Concordia diagrams and weighted mean calculations were made using Isoplot/Ex_ver3.

Zircon in situ Hf isotope analysis was carried out using a RESOlution SE 193 nm laser ablation system attached to a Thermo Fisher Scientific Neptune Plus multi collector (MC-ICP-MS). Instrumental conditions and data acquisition protocols were described by Hou et al. (2009). A stationary spot used a beam diameter of ~ 38 μm. As the carrier gas, helim was used to transport the ablated sample aerosol mixed with argon from the laser ablation cell to the MC-ICP-MS torch by a mixing chamber. ^{176}Lu/^{175}Lu = 0.02658 and ^{172}Yb/^{173}Yb = 0.796218 ratios were determined to correct for the isobaric interferences of ^{176}Lu and ^{176}Yb on ^{176}Hf. For instrumental mass bias correction, Yb isotope ratios were normalized to ^{172}Yb/^{173}Yb = 1.35274 and Hf

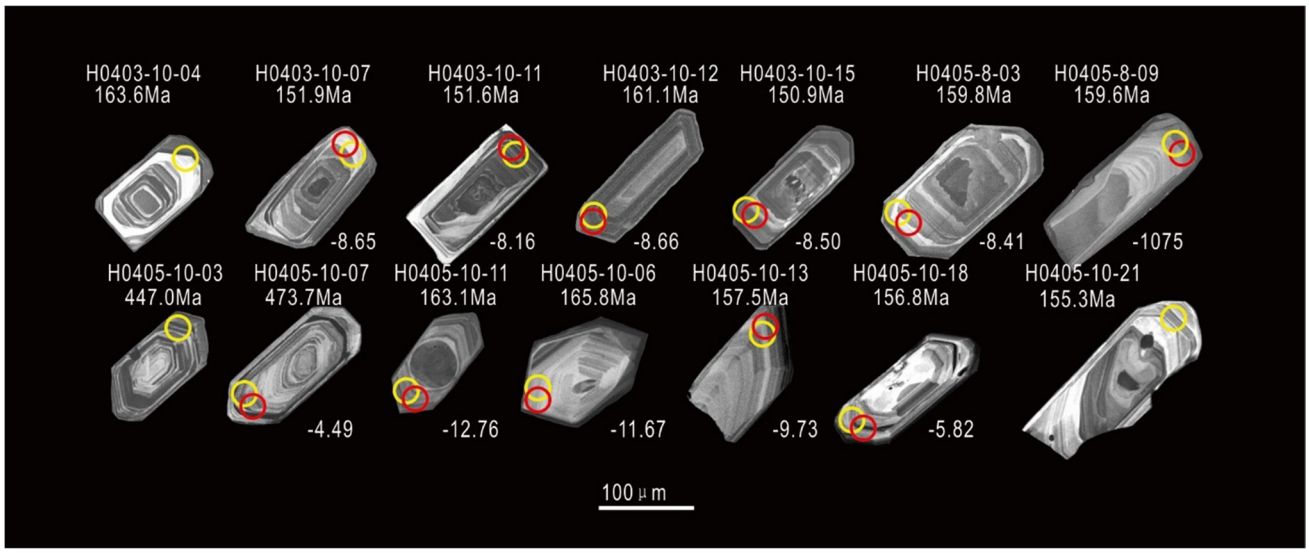

Fig. 3 Figures of the Zircon test site of samples H0403-10, H0405-10, and H0405-8. Yellow rings are the U–Pb test site and the red rings are the Hf isotope test site

isotope ratios to $^{179}Hf/^{177}Hf = 0.7325$ using an exponential law. The mass bias behavior of Lu was assumed to follow that of Yb; the mass bias correction protocol was described by Hou et al. (2007).

The major and trace element compositions were determined by X-ray fluorescence (XRF-1800, SHIMADZU) on fused glasses and inductively coupled plasma mass spectrometry (Element XR, Thermo) after acid digestion of samples in Teflon bombs. Loss on ignition was measured after heating to 1000℃ for 3 h in a muffle furnace. The precision of the XRF analyses is within ± 2% for the oxides greater than 0.5 wt.% and within ± 5% for the oxides greater than 0.1 wt.%. Sample powders (about 50 mg) were dissolved in Teflon bombs using a $HF + HNO_3$ mixture for 48 h at about 190℃. The solution was evaporated to incipient dryness, dissolved by concentrated HNO_3 and evaporated at 150℃ to dispel the fluorides. The samples were diluted to about 100 g for analysis after redissolved in 30% HNO_3 overnight.

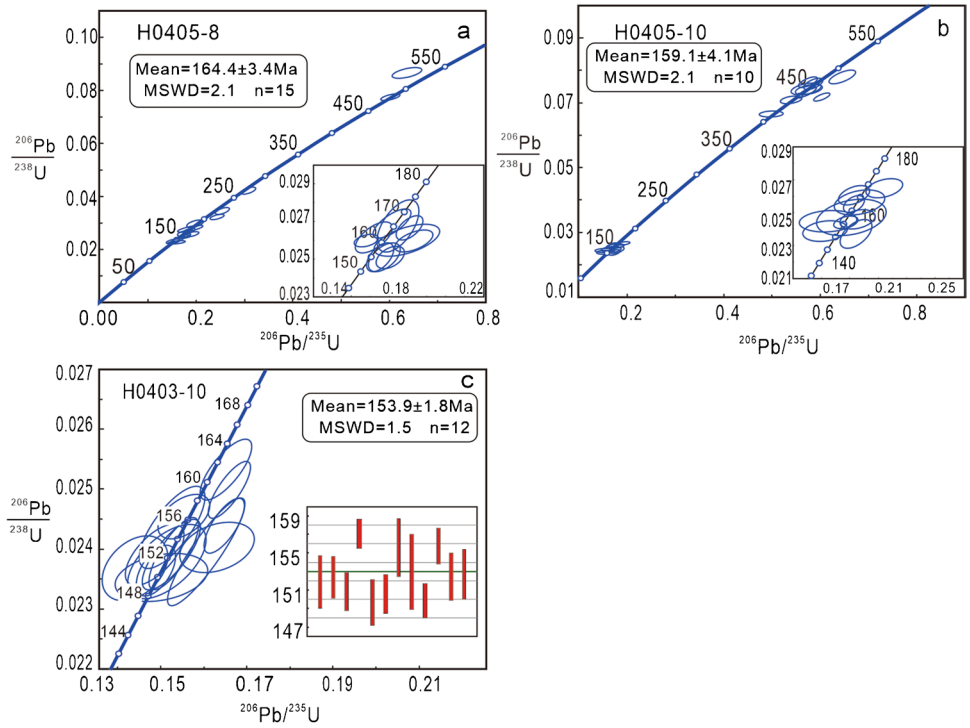

Fig. 4 Zircon U–Pb concordia diagram for samples H0403-10, H0405-10, and H0405-8 from the Guangnan pluton

Table 1 Results of Zircon U–Pb dating in granite

Sample number: H0405-10	Pb Total ppm	Th 232 ppm	U 238 ppm	$^{207}Pb/^{206}Pb$ Ratio	$^{207}Pb/^{206}Pb$ 1sigma	$^{207}Pb/^{235}U$ Ratio	$^{207}Pb/^{235}U$ 1sigma	$^{206}Pb/^{238}U$ Ratio	$^{206}Pb/^{238}U$ 1sigma	$^{238}U/^{232}Th$ Ratio	$^{207}Pb/^{206}Pb$ Age (Ma)	$^{207}Pb/^{206}Pb$ 1sigma	$^{207}Pb/^{235}U$ Age (Ma)	$^{207}Pb/^{235}U$ 1sigma	$^{206}Pb/^{238}U$ Age (Ma)	$^{206}Pb/^{238}U$ 1sigma
H0405-10–01	125.2	629.5	704.0	0.0721	0.0021	0.2683	0.0080	0.0270	0.0004	0.90	990.7	62.0	241.3	6.4	171.8	2.5
H0405-10–02	28.3	185.0	226.0	0.0350	0.0024	0.1279	0.0094	0.0265	0.0003	0.98	error	error	122.2	8.4	168.4	2.0
H0405-10–03	467.4	994.5	951.5	0.0610	0.0009	0.6033	0.0108	0.0718	0.0009	0.78	638.9	32.2	479.3	6.8	447.0	5.3
H0405-10–04	176.6	343.9	656.0	0.0569	0.0009	0.5742	0.0109	0.0732	0.0010	1.62	487.1	35.2	460.8	7.0	455.6	5.7
H0405-10–05	31.8	199.9	189.0	0.0533	0.0024	0.1935	0.0086	0.0265	0.0004	0.77	342.7	103.7	179.6	7.3	168.4	2.4
H0405-10–06	28.7	177.1	178.2	0.0484	0.0020	0.1724	0.0068	0.0261	0.0004	0.81	116.8	98.1	161.5	5.9	165.8	2.4
H0405-10–07	148.4	304.1	461.0	0.0547	0.0010	0.5748	0.0130	0.0762	0.0010	1.22	398.2	44.4	461.1	8.4	473.7	6.2
H0405-10–08	66.7	399.6	552.4	0.0490	0.0013	0.1723	0.0049	0.0255	0.0003	1.07	146.4	63.0	161.4	4.3	162.4	2.1
H0405-10–09	69.0	146.9	202.6	0.0564	0.0016	0.5764	0.0184	0.0740	0.0010	1.09	477.8	61.1	462.2	11.8	460.0	6.1
H0405-10–10	221.9	498.7	525.0	0.0560	0.0010	0.5860	0.0134	0.0758	0.0010	0.86	453.8	43.5	468.3	8.6	470.8	6.2
H0405-10–11	46.5	296.1	276.4	0.0500	0.0030	0.1758	0.0117	0.0256	0.0005	0.72	194.5	137.9	164.5	10.1	163.1	3.2
H0405-10–12	36.4	264.7	166.8	0.0460	0.0039	0.1541	0.0134	0.0245	0.0004	0.69	error		145.5	11.8	155.9	2.7
H0405-10–13	5.7	73.0	75.0	0.0490	0.0039	0.1703	0.0160	0.0247	0.0008	0.78	146.4	177.8	159.7	13.9	157.5	4.8
H0405-10–14	30.5	191.1	196.9	0.0435	0.0029	0.1546	0.0110	0.0257	0.0004	0.79	error		145.9	9.6	163.6	2.7
H0405-10–15	97.3	70.4	1141.1	0.0543	0.0017	0.4991	0.0159	0.0666	0.0005	13.00	383.4	65.7	411.1	10.8	415.9	3.2
H0405-10–16	211.5	447.0	792.0	0.0551	0.0015	0.5390	0.0141	0.0710	0.0007	1.37	416.7	54.6	437.8	9.3	442.1	4.0
H0405-10–17	99.0	220.7	279.4	0.0559	0.0020	0.5714	0.0210	0.0742	0.0012	1.01	450.0	79.6	458.9	13.6	461.7	7.1
H0405-10–18	34.7	235.7	199.3	0.0515	0.0023	0.1746	0.0082	0.0246	0.0004	0.70	261.2	105.5	163.4	7.1	156.8	2.5
H0405-10–19	30.8	188.6	252.0	0.0464	0.0036	0.1519	0.0105	0.0239	0.0004	1.06	16.8	174.1	143.6	9.2	152.2	2.6
H0405-10–20	109.3	180.1	468.6	0.0600	0.0012	0.6459	0.0179	0.0779	0.0013	2.04	605.6	47.2	505.9	11.1	483.7	8.1
H0405-10–21	57.5	318.9	674.8	0.0496	0.0016	0.1667	0.0056	0.0244	0.0003	1.76	176.0	75.9	156.6	4.9	155.3	1.6
H0405-10–22	32.8	208.0	288.2	0.0533	0.0022	0.1737	0.0073	0.0237	0.0006	1.10	342.7	88.0	162.7	6.3	151.1	3.7

Sample number: H0403-10	Pb Total ppm	Th 232 ppm	U 238 ppm	$^{207}Pb/^{206}Pb$ Ratio	$^{207}Pb/^{206}Pb$ 1sigma	$^{207}Pb/^{235}U$ Ratio	$^{207}Pb/^{235}U$ 1sigma	$^{206}Pb/^{238}U$ Ratio	$^{206}Pb/^{238}U$ 1sigma	$^{238}U/^{232}Th$ Ratio	$^{207}Pb/^{206}Pb$ Age (Ma)	$^{207}Pb/^{206}Pb$ 1sigma	$^{207}Pb/^{235}U$ Age (Ma)	$^{207}Pb/^{235}U$ 1sigma	$^{206}Pb/^{238}U$ Age (Ma)	$^{206}Pb/^{238}U$ 1sigma
H0403-10–01	156.5	867.6	1487.7	0.0509	0.0008	0.1807	0.0034	0.0257	0.0003	1.33	235.3	61.1	168.7	2.9	163.8	1.9
H0403-10–02	49.1	311.9	482.2	0.0489	0.0015	0.1617	0.0057	0.0240	0.0005	1.21	142.7	65.7	152.2	5.0	152.9	2.9

Table 1 (continued)

H0403-10–03	69.1	443.3	310.5	0.0690	0.0032	0.2175	0.0107	0.0229	0.0007	0.55	898.2	-104.6	199.8	8.9	146.0	4.1
H0403-10–04	98.5	518.4	782.6	0.0499	0.0011	0.1766	0.0042	0.0257	0.0003	1.20	187.1	19.4	165.2	3.7	163.6	1.7
H0403-10–05	96.7	539.3	839.1	0.0479	0.0013	0.1587	0.0045	0.0241	0.0004	1.24	94.5	69.4	149.6	3.9	153.4	2.3
H0403-10–06	274.8	1077.1	4184.2	0.0528	0.0008	0.1886	0.0038	0.0259	0.0004	3.38	320.4	39.8	175.5	3.2	164.9	2.3
H0403-10–07	97.2	658.2	874.2	0.0544	0.0018	0.1783	0.0061	0.0238	0.0003	1.15	390.8	71.3	166.6	5.2	151.9	2.1
H0403-10–08	114.8	689.8	1181.9	0.0484	0.0011	0.1653	0.0039	0.0248	0.0003	1.40	116.8	55.6	155.3	3.4	158.1	1.6
H0403-10–09	77.9	704.3	778.9	0.0590	0.0018	0.1657	0.0048	0.0204	0.0003	0.91	568.6	64.8	155.7	4.2	130.4	2.2
H0403-10–10	59.8	335.8	525.0	0.0455	0.0018	0.1477	0.0059	0.0237	0.0004	1.26	error		139.9	5.2	150.7	2.5
H0403-10–11	124.8	632.9	1802.0	0.0481	0.0010	0.1578	0.0036	0.0238	0.0003	2.30	101.9	46.3	148.8	3.2	151.6	2.1
H0403-10–12	222.8	843.5	3539.0	0.0504	0.0008	0.1756	0.0031	0.0253	0.0004	3.30	216.7	38.9	164.3	2.7	161.1	2.3
H0403-10–13	63.0	265.1	996.6	0.0479	0.0010	0.1628	0.0051	0.0246	0.0005	3.01	94.5	51.8	153.2	4.4	156.6	3.2
H0403-10–14	199.9	895.9	3954.6	0.0511	0.0007	0.1707	0.0052	0.0242	0.0006	3.57	255.6	29.6	160.1	4.5	154.0	4.0
H0403-10–15	32.3	174.5	291.9	0.0490	0.0020	0.1602	0.0068	0.0237	0.0003	1.32	146.4	94.4	150.9	5.9	150.9	1.9
H0403-10–16	222.7	699.3	3871.6	0.0515	0.0010	0.1744	0.0030	0.0246	0.0003	4.41	264.9	44.4	163.3	2.6	156.8	1.9
H0403-10–17	140.8	728.8	1575.2	0.0486	0.0010	0.1617	0.0046	0.0241	0.0004	1.70	127.9	50.0	152.2	4.0	153.5	2.6
H0403-10–18	135.4	667.3	1646.2	0.0490	0.0009	0.1628	0.0038	0.0241	0.0004	1.95	146.4	44.4	153.1	3.3	153.7	2.7
H0403-10–19	56.5	290.4	620.8	0.0546	0.0029	0.1712	0.0083	0.0228	0.0003	1.69	394.5	118.5	160.5	7.2	145.1	2.1
H0403-10–20	50.0	232.1	398.0	0.0539	0.0019	0.2091	0.0075	0.0281	0.0007	1.35	368.6	86.1	192.8	6.3	178.9	4.2
Sample number: H0405-8	Pb Total ppm	Th 232 ppm	U 238 ppm	$^{207}Pb/^{206}Pb$ Ratio	$^{207}Pb/^{206}Pb$ 1sigma	$^{207}Pb/^{235}U$ Ratio	$^{207}Pb/^{235}U$ 1sigma	$^{206}Pb/^{238}U$ Ratio	$^{206}Pb/^{238}U$ 1sigma	$^{238}U/^{232}Th$ Ratio	$^{207}Pb/^{206}Pb$ Age (Ma)	$^{207}Pb/^{206}Pb$ 1sigma	$^{207}Pb/^{235}U$ Age (Ma)	$^{207}Pb/^{235}U$ 1sigma	$^{206}Pb/^{238}U$ Age (Ma)	$^{206}Pb/^{238}U$ 1sigma
H0405-8–01	300.7	555.7	645.8	0.0565	0.0012	0.6047	0.0135	0.0775	0.0007	0.99	472.3	44.4	480.2	8.5	481.5	4.4
H0405-8–02	58.8	300.1	492.5	0.0489	0.0014	0.1813	0.0061	0.0269	0.0005	1.35	142.7	66.7	169.1	5.3	170.9	3.0
H0405-8–03	130.7	693.7	1495.8	0.0511	0.0010	0.1773	0.0055	0.0251	0.0005	1.73	255.6	50.9	165.7	4.7	159.8	3.2
H0405-8–04	124.8	727.2	1130.3	0.0478	0.0014	0.1723	0.0062	0.0262	0.0005	1.40	87.1	75.0	161.4	5.4	166.6	3.3
H0405-8–05	364.5	1410.1	2879.0	0.0551	0.0016	0.2451	0.0094	0.0322	0.0007	1.62	416.7	66.7	222.6	7.7	204.3	4.4
H0405-8–06	477.2	1542.5	5331.5	0.0692	0.0017	0.2275	0.0101	0.0237	0.0007	2.77	905.6	50.8	208.1	8.4	151.1	4.2
H0405-8–07	67.8	409.4	385.0	0.0499	0.0031	0.1980	0.0115	0.0295	0.0008	0.74	187.1	144.4	183.5	9.8	187.5	5.2
H0405-8–08	474.3	2208.9	5764.7	0.0520	0.0008	0.1909	0.0041	0.0266	0.0005	2.13	287.1	35.2	177.4	3.5	169.2	3.0
H0405-8–09	231.8	834.2	5034.0	0.0507	0.0009	0.1755	0.0047	0.0251	0.0005	6.04	227.8	44.4	164.2	4.1	159.6	3.2

Table 1 (continued)

H0405-8–10	160.1	960.5	1555.4	0.0533	0.0028	0.1906	0.0107	0.0260	0.0006	1.20	342.7	118.5	177.2	9.1	165.2	3.9	
H0405-8–11	155.4	341.0	2173.8	0.0532	0.0013	0.3086	0.0093	0.0422	0.0009	5.28	344.5	55.6	273.1	7.2	266.2	5.8	
H0405-8–12	253.6	257.1	1452.6	0.0532	0.0014	0.6372	0.0202	0.0865	0.0012	4.48	338.9	61.1	500.6	12.6	534.9	7.0	
H0405-8–13	308.3	625.8	793.9	0.0912	0.0031	0.9120	0.0292	0.0735	0.0019	1.38	1450.0	68.7	658.1	15.5	457.0	11.2	
H0405-8–14	399.7	965.4	6704.8	0.0498	0.0011	0.1844	0.0077	0.0268	0.0009	5.50	187.1	19.4	171.8	6.6	170.3	5.8	
H0405-8–15	466.5	292.8	1367.7	0.0818	0.0026	1.0822	0.0308	0.0961	0.0014	3.74	1240.4	56.5	744.7	15.0	591.7	8.3	
H0405-8–16	243.2	925.6	4893.7	0.0521	0.0012	0.1805	0.0048	0.0251	0.0004	5.15	287.1	53.7	168.5	4.1	159.9	2.3	
H0405-8–17	122.3	620.2	976.6	0.0541	0.0018	0.1933	0.0067	0.0259	0.0004	1.31	376.0	78.7	179.4	5.7	165.1	2.5	
H0405-8–18	226.6	956.1	4210.5	0.0483	0.0012	0.1622	0.0044	0.0243	0.0003	3.87	122.3	57.4	152.7	3.8	155.1	2.0	
H0405-8–19	96.8	469.8	753.9	0.0501	0.0045	0.1875	0.0160	0.0277	0.0009	1.33	198.2	196.3	174.5	13.7	176.3	5.4	
H0405-8–20	26.6	166.5	237.8	0.0493	0.0034	0.1537	0.0093	0.0232	0.0005	1.15	164.9	151.8	145.2	8.2	147.9	2.9	

An internal standard solution containing the element Rh was used to monitor signal drift during analysis. Analytical results for USGS standards indicated that the uncertainties for most elements were within 5%.

Results

Zircon U–Pb dating

Coarse-grained porphyritic biotite granite (sample H0405-8) Zircon grains in sample H0405-8 are euhedral, with the lengths of 100 to 150 μm and the length/width ratio of 1.5 to 4. It can be found that some grains are fine oscillatory growth zoning from the CL images (Fig. 4a). $^{232}Th/^{238}U$ ratios range from 0.14 to 1.06. All the characteristics indicate they are formed by the magmatic origin. There were 23 zircons tested, and all of them were analyzed at the edge of single-grain zircon (Fig. 3). The test data results are presented in Table 1. The results of H0405-8–06, H0405-8–13, and H0405-8–15 were abandoned because of their serious signal loss leading harmony degree less than 90%. The results of H0405-8–01 (481.5 Ma) and H0405-8–12 (534.9 Ma) are significantly older; these features can be interpreted as captured Caledonian magmatic zircons during Jurassic magmatic activity. The results of H0405-8–05 (204.3 Ma), H0405-8–11 (266.2 Ma), and H0405-8–12 (218.4 Ma) can be interpreted as captured Caledonian and Indosinian magmatic zircons during Jurassic magmatic activity. The results data showed that the 15 points are plotted on or close to the coordination line in the coordination diagram (Fig. 4a), with weighted mean age at 164.4 ± 3.4 Ma (MSWD = 2.1, n = 15, confidence 95% (Fig. 4c)), which can be interpreted as crystallization age of the rock.

Two-mica granite (sample H0405-10) Zircon grains of sample H0405-10 are euhedral, with the lengths of 80 to 150 μm and the length/width ratio of 1.5 to 3. It can be found that some grains are fine oscillatory growth zoning from the CL images (Fig. 4a). $^{232}Th/^{238}U$ ratios range from 0.53 to 1.59. There were 22 zircons tested, and all of them were analyzed at the edge of single-grain zircon. H0405-10–1, H0405-10–2, and H0405-10–14 were abandoned because of their serious signal loss leading harmony degree less than 90%. The results data showed that the 19 points are plotted on or close to the coordination line in the coordination diagram (Fig. 4b). Based on the age results, the zircon ages can be divided into two groups. The $^{206}Pb/^{238}U$ ages of the first group yield between 151.1 and 168.4 Ma, with weighted mean age at 159.1 ± 4.1 Ma (MSWD = 5.4, n = 10.95% confidence) (Fig. 4a), which can be interpreted as crystallization age of the rock. The second group yield between 483.7

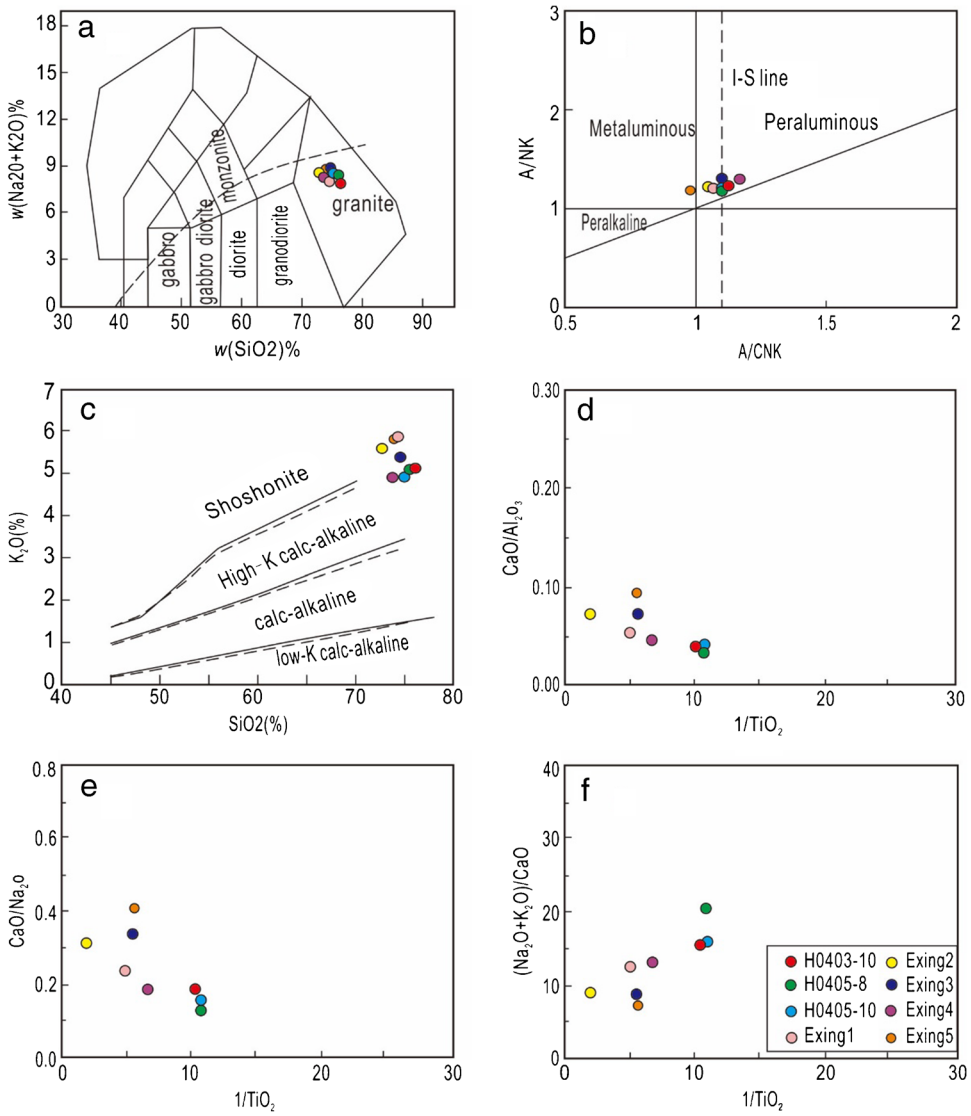

Fig. 5 **a** Diagrams of TAS (modified after Middlemost 1994), **b** A/CNK vs. A/NK (after Maniar and Piccolli 1989), **c** Amazonia silica-rich granite bodies (modified after Frost et al. 2016), **d** CaO/Al_2O_3 vs. $1/TiO_2$, **e** CaO/Na_2O vs. $1/TiO_2$, and **f** $(Na_2O+K_2O)/CaO$ vs. $1/TiO_2$ (modified after Sun 2018. Exing 1 to Exing 5 based on 1:200,000 regional geological survey report 1969)

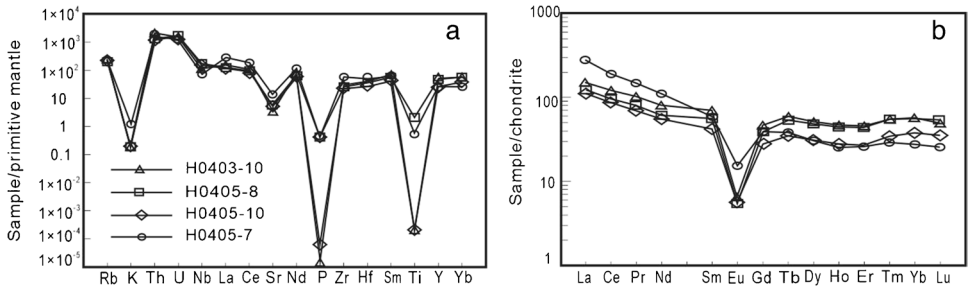

Fig. 6 **a** primitive mantle-normalized element spider diagram, normalizing values from Sun and McDonough (1989); **b** Chondrite-normalized REE patterns for the Guangnan pluton, normalizing values from Sun and McDonough (1989)

and 415.9 Ma including spots H0405-10–03, H0405-10–04, H0405-10–07, H0405-10–09, H0405-10–10, H0405-10–13, H0405-10–16, H0405-10–17, and H0405-10–20. These ages, compared with the first group, are significantly older, and these zircons showed many fine oscillation rings. The features can be interpreted as captured Caledonian magmatic zircons during Jurassic magmatic activity.

Biotite granite (sample H0403-10) Zircon grains of sample H0405-10 are euhedral, with the lengths of 200 to 500 μm and the length/width ratio of 1.5 to 3. It can be found that some grains are fine oscillatory growth zoning from the CL images (Fig. 4a). $^{232}Th/^{238}U$ ratios range from 0.23 to 1.43. There were 20 zircons tested and were analyzed at the edge of single-grain zircon. H0403-10–03, H0403-10–09,

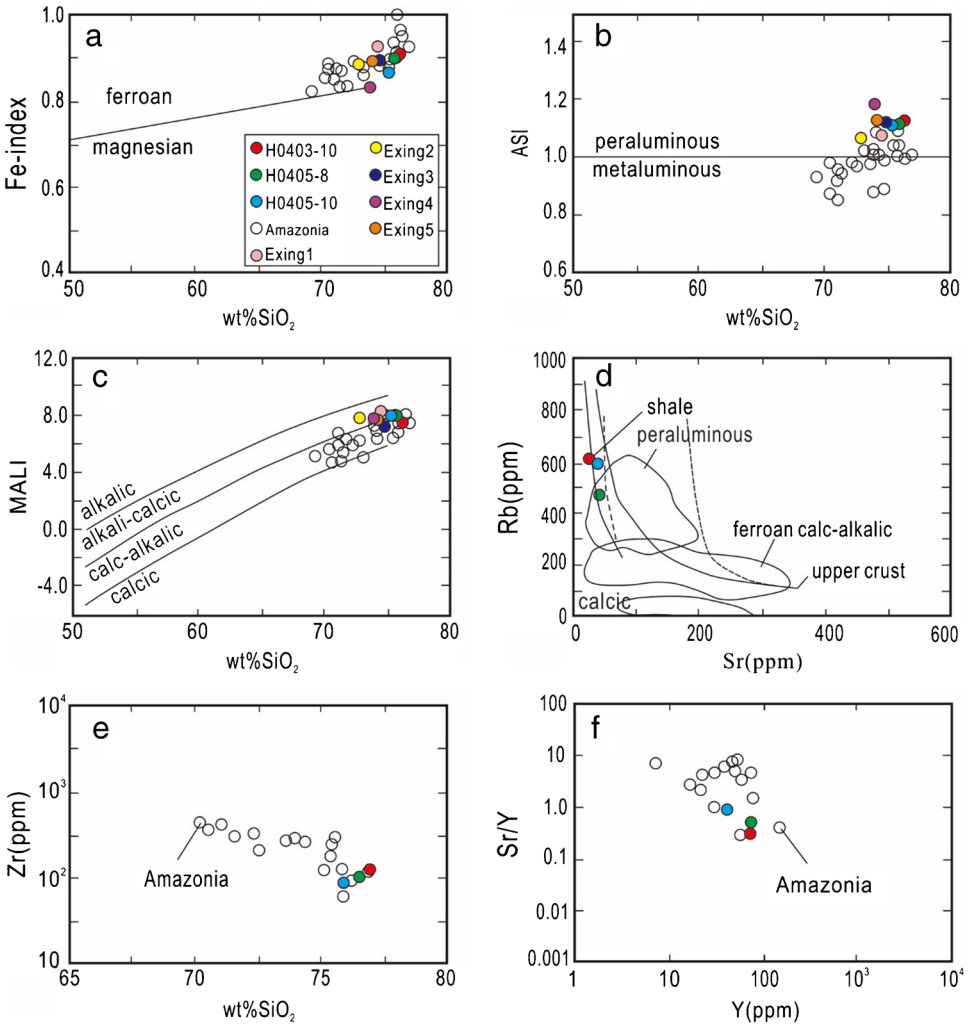

Fig. 7 Diagrams of the Guangnan and Amazonia silica-rich granite bodies (modified after Frost et al. 2016). (a), (b), (c), (d), (e), and (f) are the diagrams of Fe index vs. SiO_2 (wt.%), ASI vs. SiO_2 (wt.%), MALI vs. SiO_2 (wt.%), Rb (ppm) vs. Sr (wt.%), Zr (ppm) vs. SiO_2 (wt.%), and Sr/Y vs. Y (ppm), respectively

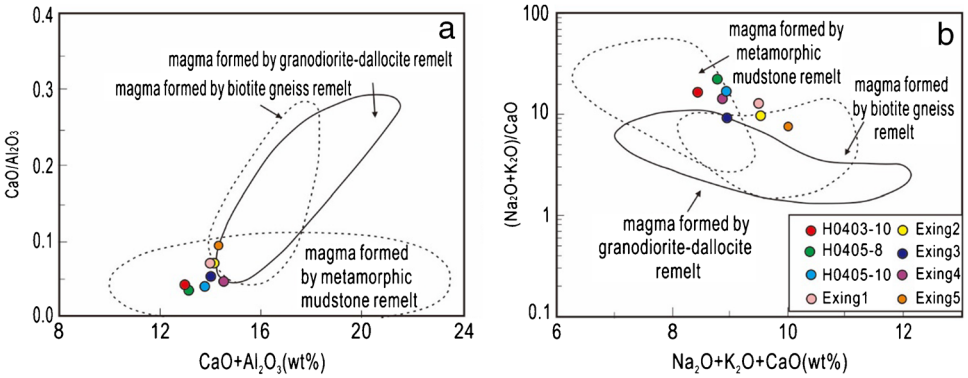

Fig. 8 Diagrams of CaO/Al_2O_3 vs. ($CaO + Al_2O_3$) (**a**) and ($Na_2O + K_2O$)/CaO vs. ($Na_2O + K_2O + CaO$) (**b**) (modified after Sun 2018)

H0403-10–19, and H0403-10–20 were abandoned because of their serious signal loss leading harmony degree less than 90%. The results data showed that the 16 points are plotted on or close to the coordination line in the coordination diagram (Fig. 4c). Based on the age results, the $^{206}Pb/^{238}U$ ages of the 16 points yield between 150.7 and 163.8 Ma, with weighted mean age at 153.9 ± 1.8 Ma (MSWD = 1.5, $n = 16$, the reliability is 95% confidence (Fig. 4b)), which can be interpreted as crystallization age of the rock. The second group yield between 483.7 and 415.9 Ma including spots H0405-10–03, H0405-10–04, H0405-10–07, H0405-10–09, H0405-10–10, H0405-10–13, H0405-10–16, H0405-10–17, and H0405-10–20. These ages, compared with the first group, are significantly older, and these zircons showed

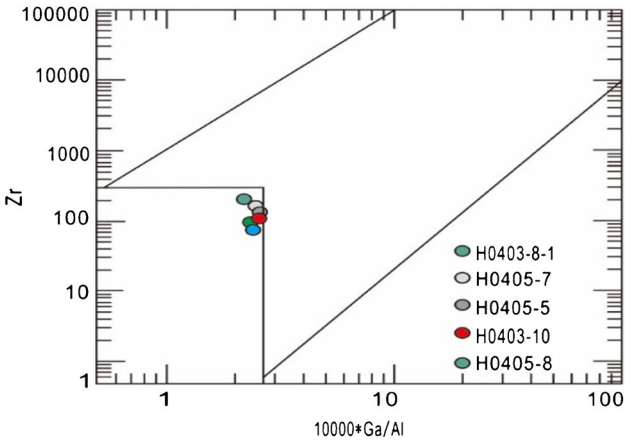

Fig. 9 Diagrams of the Zr vs. 10000*Ga/Al from Guangnan pluton (modified after Sami et al. 2017)

many fine oscillation rings. The features can be interpreted as captured Caledonian magmatic zircons during Jurassic magmatic activity (Figs. 5,6,7,8,9).

Zircon Lu–Hf isotope analysis

The zircon Lu–Hf isotopic test results of the Guangnan pluton are shown in Table 2. The measured $^{176}Lu/^{177}Hf$ ratio (< 0.002) of the three samples can represent the Hf isotope composition characteristics during the formation of zircon.

Sample H0405-10 tested 12 spots; the initial ratio of ($^{176}Hf/^{177}Hf$), the $\varepsilon_{Hf}(t)$ value, age of the first-stage Hf model T_{DM1}, and the age of second-stage Hf model T_{DM2} yielded at 0.282294–0.282426, − 3.94– − 11.67, 1157–1344 Ma, and 1729–2060 Ma, respectively. Sample H0403-10 tested 13 spots. The initial ratio of ($^{176}Hf/^{177}Hf$), the $\varepsilon_{Hf}(t)$ value, age of the first-stage Hf model T_{DM1}, and the age of second-stage Hf model T_{DM2} yielded at 0.282364–0.282469, − 7.45– − 11.13, 1115–1268 Ma, and 1677–1910 Ma, respectively. Sample H0405-8 tested 13 spots. The initial ratio of ($^{176}Hf/^{177}Hf$), the $\varepsilon_{Hf}(t)$ value, age of the first-stage Hf model T_{DM1}, and the age of second-stage Hf model T_{DM2} yielded at 0.282373–0.282446, − 8.41– − 10.75, 1212–1289 Ma, and 1740–1889 Ma, respectively. The Hf isotope two-stage model age T_{DM2} values of the three samples fall between Early Proterozoic and Mesoproterozoic (Fig. 10).

Major and trace elements

The major and trace elements of the Guangnan pluton are shown in Table 3.

The major elements show they are higher SiO_2 (72.82–76.16 wt.%), K_2O (4.91–5.85 wt.%), Na_2O (2.68–3.50 wt.%), Al_2O_3 (12.49–13.92 wt.%), lower ZrO_2 (83.5–118 ug/g), TiO_2 (0.09–0.52 wt.%), Fe_2O_3 (0.03–0.93 wt.%), FeO (0.35–2.64 wt.%), MgO (0.10–0.42 wt.%), MnO (0.03–0.12 wt.%), and CaO (0.42–1.21 wt.%). K_2O/Na_2O ratios range from 1.41 to 2.01; total alkali contents range from 7.95 to 8.82%. The values of DI range from 88.46 to 94.84, and the AR range from 2.43 to 3.07. The samples are located in the granite area on the diagram of TAS (Fig. 5a), and located in the high potassium calcium-alkaline series area on the SiO_2-K_2O diagram (Fig. 5b). The value of A/CNK ranges from 0.98 to 1.12 (Table 3, Fig. 5b), and most of them are greater than 1, belonging to peraluminous granite. The Guangnan pluton further classified as ferrous, calcareous-alkali-calcium sample in the SiO_2-FeO* diagram and SiO_2-alkali-calcium index of magma (MALI) diagram, respectively (Fig. 7a and c).

The rare earth element distribution pattern of the Guangnan pluton sample has obvious negative Eu anomalies, showing a right-leaning "V"-shaped characteristic, and the middle rare earth elements are not enriched relative to the heavy rare earth elements (Fig. 6a). In the spider web diagram of trace elements, the Guangnan granite samples are enriched in Rb, Th, U, Nb, and light rare earth elements, and are obviously depleted in Ba, Sr, P, and Ti (Fig. 6b).

Discussion

Time of Guangnan pluton intrusion

The Zhuguangshan batholith is composed of multiple Caledonian, Indosinian, and Yanshanian granitic rocks (Li 1990), and the Yanshanian plutons are mainly distributed in the southern body; therefore, few chronological studies were done on the Yanshanian plutons exposed in the northern Zhuguangshan batholith. Zheng (1988) reported the Rb–Sr isochronal age of 157 Ma and the mica Ar–Ar age of 152 Ma from the Guangnan biotite granite in the Exing area. Li (1990) analyzed single-grain zircon U–Pb from the biotite granite in the Exing area yielded at 155.5 Ma. Guo et al. (2017) conducted SHRIMP U–Pb age dating on the two-mica granite from Dongluo county, and yielded at 148.2 Ma.

This paper studied the biotite granite and found that the pluton formed at 164.4 M in Exing area. Compared with the studies of Zheng (1988) and Li (1990), the result of this paper is slightly earlier. The two-mica granite of Exing area formed 159.1 Ma on the southwest, the biotite granite in the Shanggushi area formed 153.9 Ma, and the two-mica granite from the Dongluo area formed 148.2 Ma (Guo et al. 2017). The ages of Guangnan pluton show that the pluton is gradually getting younger from the northeast to the southwest. Considering analyzed multiple factors acted on previous studies, it is deduced that the Guangnan pluton may intrude during 164 Ma and 148 Ma, that is, the Guangnan pluton formed in the late Middle Jurassic to the Late Jurassic period.

Table 2 Results of Zircon Lu–Hf isotopes in granite

	Age (Ma)	$^{176}Yb/^{177}Hf$	$^{176}Lu/^{177}Hf$	2σ	$^{176}Hf/^{177}Hf$	2σ	I_{Hf}	$\varepsilon_{Hf}(0)$	$\varepsilon_{Hf}(t)$	T_{DM}	T_{DMc}	$f_{Lu/Hf}$
Sample number: H0405-10												
H0405-10–5	168.4	0.025011	0.000898	0.000029	0.282409	0.000016	0.282406	−12.84	−9.25	1187	1801	-0.97
H0405-10–6	165.8	0.016505	0.000587	0.000009	0.282341	0.000017	0.282339	−15.24	−11.67	1271	1952	-0.98
H0405-10–7	473.7	0.023603	0.000861	0.000006	0.282358	0.000015	0.28235	−14.64	−4.49	1256	1729	-0.97
H0405-10–8	162.4	0.020192	0.000829	0.000021	0.282294	0.000026	0.282292	−16.90	−13.41	1344	2060	-0.98
H0405-10–9	460.0	0.032705	0.001143	0.000006	0.282384	0.000018	0.282374	−13.72	−3.94	1229	1684	-0.97
H0405-10–10	470.8	0.029956	0.001086	0.000024	0.282337	0.000016	0.282327	−15.40	−5.37	1294	1783	-0.97
H0405-10–11	163.1	0.014218	0.000511	0.000012	0.282312	0.000025	0.28231	−16.27	−12.76	1309	2019	-0.98
H0405-10–12	155.9	0.045071	0.001564	0.000068	0.282405	0.000015	0.2824	−12.99	−9.73	1214	1822	-0.95
H0405-10–13	157.5	0.020740	0.000704	0.000014	0.282426	0.000016	0.282424	−12.25	−8.85	1157	1768	-0.98
H0405-10–17	461.7	0.030424	0.001081	0.000015	0.282330	0.000016	0.28232	−15.64	−5.82	1303	1803	-0.97
H0405-10–18	156.8	0.019608	0.000683	0.000007	0.282367	0.000020	0.282365	−14.33	−10.95	1238	1900	-0.98
H0405-10–19	152.2	0.030014	0.001037	0.000010	0.282393	0.000020	0.28239	−13.39	−10.17	1213	1846	-0.97
Sample number: H0403-10												
H0403-10–2	152.9	0.027933	0.000996	0.000009	0.282398	0.000017	0.282395	−13.22	−9.98	1205	1835	-0.97
H0403-10–5	153.4	0.036624	0.001274	0.000004	0.282467	0.000030	0.282463	−10.80	−7.56	1117	1682	-0.96
H0403-10–7	151.9	0.040106	0.001387	0.000005	0.282437	0.000017	0.282433	−11.86	−8.65	1163	1751	-0.96
H0403-10–8	158.1	0.040763	0.001363	0.000036	0.282417	0.000018	0.282413	−12.57	−9.22	1191	1793	-0.96
H0403-10–10	150.7	0.022261	0.000824	0.000009	0.282456	0.000018	0.282453	−11.18	−7.97	1119	1706	-0.98
H0403-10–11	151.6	0.046328	0.001531	0.000020	0.282451	0.000017	0.282447	−11.35	−8.16	1147	1720	-0.95
H0403-10–12	161.1	0.038008	0.001359	0.000017	0.282431	0.000014	0.282427	−12.05	−8.66	1170	1758	-0.96
H0403-10–13	156.6	0.040294	0.001472	0.000015	0.282364	0.000013	0.28236	−14.42	−11.13	1268	1910	-0.96
H0403-10–14	154.0	0.095395	0.003013	0.000033	0.282459	0.000014	0.28245	−11.09	−8.01	1184	1712	-0.91
H0403-10–15	150.9	0.015126	0.000542	0.000002	0.282440	0.000015	0.282438	−11.76	−8.50	1133	1740	-0.98
H0403-10–16	156.8	0.032484	0.001179	0.000011	0.282458	0.000011	0.282454	−11.11	−7.80	1127	1700	-0.96
H0403-10–17	153.5	0.022936	0.000828	0.000003	0.282436	0.000015	0.282434	−11.89	−8.58	1147	1749	-0.98
H0403-10–18	153.7	0.037236	0.001317	0.000014	0.282469	0.000015	0.282466	−10.71	−7.45	1115	1677	-0.96
Sample number: H0405-8												
H0405-8–2	0.107791	0.002962	0.003827	0.000088	0.282421	0.000017	0.282409	−12.41	−9.09	1268	1792	-0.88
H0405-8–3	0.127819	0.004870	0.003941	0.000141	0.282446	0.000021	0.282435	−11.51	−8.41	1233	1740	-0.88
H0405-8–4	0.038619	0.001221	0.001438	0.000048	0.282392	0.000024	0.282387	−13.45	−9.96	1228	1843	-0.96
H0405-8–8	0.130389	0.002638	0.004151	0.000072	0.282415	0.000016	0.282402	−12.63	−9.37	1289	1808	-0.87
H0405-8–9	0.038188	0.000594	0.001228	0.000016	0.282373	0.000014	0.282369	−14.12	−10.75	1248	1889	-0.96
H0405-8–10	0.048118	0.001022	0.001691	0.000034	0.282382	0.000015	0.282377	−13.78	−10.34	1250	1867	-0.95
H0405-8–16	0.060346	0.001757	0.002190	0.000082	0.282399	0.000021	0.282393	−13.18	−9.89	1243	1836	-0.93
H0405-8–17	0.076184	0.001137	0.002516	0.000029	0.282428	0.000017	0.28242	−12.16	−8.82	1212	1771	-0.92
H0405-8–18	0.074921	0.003634	0.002413	0.000108	0.282420	0.000013	0.282414	−12.43	−9.26	1219	1791	-0.93
H0405-8–19	0.061153	0.000524	0.002068	0.000013	0.282411	0.000013	0.282405	−12.76	−9.11	1221	1798	-0.94
H0405-8–2	0.107791	0.002962	0.003827	0.000088	0.282421	0.000017	0.282409	−12.41	−9.09	1268	1792	-0.88
H0405-8–3	0.127819	0.004870	0.003941	0.000141	0.282446	0.000021	0.282435	−11.51	−8.41	1233	1740	-0.88
H0405-8–4	0.038619	0.001221	0.001438	0.000048	0.282392	0.000024	0.282387	−13.45	−9.96	1228	1843	-0.96

$\varepsilon_{Hf}(0)=[(^{176}Hf/^{177}Hf)_S/(^{176}Hf/^{177}Hf)_{CHUR,0}-1]\times10000$, $f_{Lu/Hf}=(^{176}Lu/^{177}Hf)_S/(^{176}Lu/^{177}Hf)_{CHUR}-1$, $\varepsilon_{Hf}(t)=((^{176}Hf/^{177}Hf)_S-(^{176}Lu/^{177}Hf)_S\times(e^{\lambda t}-1))/((^{176}Hf/^{177}Hf)_{CHUR,0}-(^{176}Lu/^{177}Hf)_{CHUR}\times(e^{\lambda t}-1))-1)\times10000$, $T_{DM1}(Hf)=1/\lambda\times\ln\{1+[[(^{176}Hf/^{177}Hf)_S-(^{176}Hf/^{177}Hf)_{DM}]/[[(^{176}Hf/^{177}Hf)_S-[(^{176}Hf/^{177}Hf)_{DM}]\}$, $T_{DM2}(Hf)=T_{DM1}(Hf)-(T_{DM1}(Hf)-t)((f_{CC}-f_S)/(f_{CC}-f_{DM}))$. $(^{176}Lu/^{177}Hf)_S$ and $(^{176}Hf/^{177}Hf)_S$ is dating number, $(^{176}Lu/^{177}Hf)_{CHUR}=0.0332$、$(^{176}Hf/^{177}Hf)_{CHUR,0}=0.282772$ (Blichert-Toft and Albarède 1997), $(^{176}Lu/^{177}Hf)_{DM}=0.0384$, $(^{176}Hf/^{177}Hf)_{DM}=0.28325$ (Griffin et al. 2000), $f_{CC}=-0.548$ (continental crust $f_{Lu/Hf}$), $f_{DM}=0.16$(depleted mantle $f_{Lu/Hf}$), t=Crystallization time of Zircon, $\lambda=1.865\times10^{-11}$ yr^{-1} (Soderlund et al. 2004)

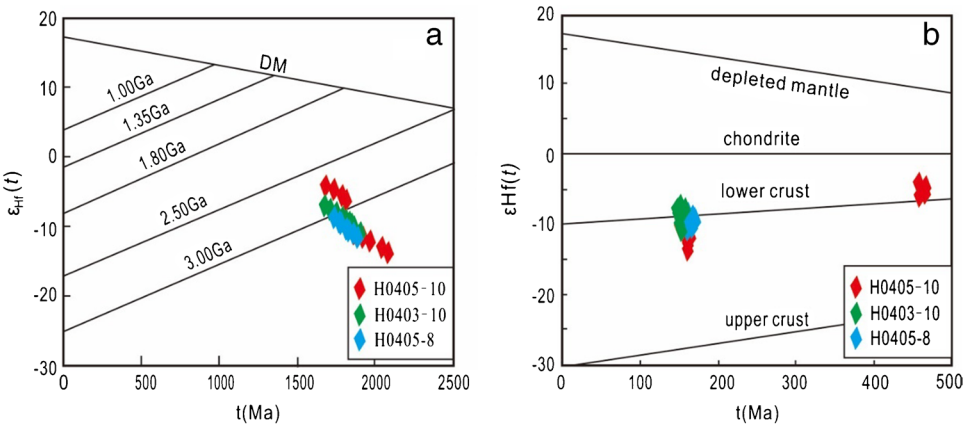

Fig. 10 Diagrams of the ε_{Hf} (t)-t (5a, 5b) from Guangnan pluton (modified after Zhou 2007)

In this study, the Zircon LA-ICP-MS U–Pb age characteristics of the pluton show that the granitic magma intrusive activity can be divided into four stages (Fig. 1c). The first stage was represented by the magma intruded into the northeast of the Exing area earlier than 164 Ma forming coarse-grained porphyritic biotite granite. The second stage can be recognized as the formation of the two-mica granite intrusion at 159 Ma in the southwest of the Exing area. The third stage was represented by the magma intruded into the Shanggushi area at 154 Ma and formed a biotite granite. The last stage magmatic activity occurred in the Dongluo area, forming two-mica granite 148 Ma (Guo et al. 2017). The time interval between each intrusion is about 5–6 Myr. Spatially, intrusive activities migrated from the northeast (Exing area) to the southwest (Shanggushi-Dongluo area). Therefore, the Guangnan pluton is a compound pluton finally formed after 4 pulsating magma intrusions and lasted about 17 Myr. According to lithological changes, it can be divided into early magmatic (Middle Jurassic 164–159 Ma) stage and late magmatic (153–148 Ma) stage. In each stage, the biotite granite is followed by two-mica granite.

Genesis of the Guangnan granites

The lack of "low-evolved" granite samples with $SiO_2 < 70$ wt.% has brought great difficulties to the interpretation of high-silica granites genesis in Guangnan area. Although the Guangnan granite was plotted in the iron region of the SiO_2-FeO* diagram (Fig. 7a), its composition is close to the "haplogranite" due to its high SiO_2 content (almost all samples $SiO_2 > 73$ wt.%). In this case, it is failed to use the S-I-M-A "letter" classification of granite (Wang 2008a; Frost et al. 2016; Garcia-Arias 2020; Miller et al. 2020). Besides, in view of the lower Zr content of the Guangnan pluton, the Guangnan high-silica granite was not considered A-type granite (Tong and Wang 2013; Wang 2008b; Wang et al. 2013, Sami et al. 2017). Guangnan high-silica granites can be classified high-silicon peraluminous light-colored granites or ferroan calc-alkaline (Ferroan calc-alkaline) high-silica granites, or muscovite-containing peraluminous granite (MPG) type granite classified by Barbarin (1999) because of its peraluminous (ASI > 1), high SiO_2 (> 72 wt.%), and low total mafic oxides ($Fe_2O_3 + FeO + MnO + MgO + TiO_2 < 5$ wt.%) characteristics (Garcia-Arias 2020; Frost et al. 2001, 2016) (Fig. 6). The rocks are located in the metamorphic mudstone-derived melt zone and the overlapping area among metapelitic rock-derived melt zone, biotite gneisses-derived melt zone, and granodiorite-dacite-derived melt zone on the diagrams of ($CaO + Al_2O_3$) vs. (CaO/Al_2O_3) and ($Na2O + K2O + CaO$) vs. ($Na_2O + K_2O$)/CaO (Fig. 8a and b). The characteristics show that the Guangnan high-silica granite may be derived from the partial melting of metapelitic rocks, but also cannot eliminate the possibility of being derived from the partial melting of biotite gneiss or granodiorite-diarrhea. The Zr vs. Ga/Al diagram (Fig. 9) confirms the rocks are I- or S-type. These results are consistent with that of Rb vs. Sr on Fig. 7d and Fig. 8a. The characteristics of low Sr and Eu negative anomalies show that plagioclase maintained in the residual phase or crystalline phase combination in equilibrium with the melt. Since amphibole was not found in the Guangnan biotite granite, it is deduced that the water content of the magma is less than 3–4 wt.% according to the phase diagram (Naney 1983; Lu et al. 2015), and the Guangnan pluton can be considered the product of partial melting of the lower crustal rocks.

The characteristics of the Middle and Late Jurassic granites in the Nanling area, including the Guangnan pluton, were high Sr/Y and La/Yb ratios. Its reason is the source rocks of these high-silica granites which have a high content of SiO_2, and the high-silica granites are mainly composed of metamorphic rocks, biotite gneiss, and granodiorite-diarrhea. A large number of previous partial melting experimental results show that the stable pressure range of plagioclase is larger than that of basic source rocks during the intermediate-acid source rocks partial melting with water

Table 3 Results of major and trace elements

Sample number	SiO_2 (%)	TiO_2 (%)	Al_2O_3 (%)	TFe_2O_3 (%)	FeO (%)	MnO (%)	MgO (%)	CaO (%)	Na_2O (%)	K_2O (%)	P_2O_5 (%)	LOI	Total (wt.%)	AR	DI	R1	R2	ACNK	FeO*	MALI
H0405-10	75.170	0.093	13.240	1.130	0.640	0.093	0.161	0.527	3.500	4.950	0.076	1.070	100.010	3.07	93.53	2595	326	1.10	0.863	7.92
H0403-10	76.160	0.097	12.490	1.150	0.440	0.036	0.101	0.514	2.820	5.130	0.020	1.440	99.958	2.53	93.73	2882	308	1.12	0.911	7.44
H0405-8	75.760	0.093	12.780	1.220	0.350	0.063	0.124	0.410	3.240	5.120	0.051	1.110	99.971	2.93	94.47	2700	303	1.10	0.899	7.95
Exing1	74.460	0.200	13.310	0.930	1.510	0.040	0.180	0.700	2.970	5.850	0.030	0.580	99.250	2.47	91.85	2504	344	1.06	0.929	8.12
Exing2	72.820	0.520	13.230	0.790	2.640	0.040	0.420	0.940	2.980	5.620	0.130	0.800	98.290	2.45	88.46	2442	380	1.04	0.899	7.66
Exing 3	74.780	0.180	13.100	0.690	1.830	0.100	0.300	0.910	2.680	5.380	0.080	0.420	98.620	2.24	89.65	2748	369	1.10	0.891	7.15
Exing 4	73.900	0.150	13.920	0.430	1.220	0.120	0.320	0.620	3.360	4.910	0.100	0.660	98.490	2.72	91.51	2590	359	1.16	0.834	7.65
Exing 5	74.100	0.180	13.105	0.030	2.150	0.040	0.260	1.210	2.980	5.820	0.750	0.580	99.055	2.43	90.98	2495	397	0.98	0.893	7.59

Sample number	Rb	Ba	Th	U	Nb	La	Ce	Sr	Nd	P	Zr	Hf	Sm	Ti	Ga	Pb
H0405-10	591	105	34.5	12.8	38.6	26.7	53.5	39.2	25.4	0.076	83.5	2.93	6.49	0.093	22.1	68.8
H0403-10	609	103	61.6	12.6	26.7	36	66.5	24.5	37.6	0.02	118	4.28	10.8	0.097	23.5	57
H0405-8	471	39.5	36.9	13.1	42.3	29.8	58.9	39.5	29	0.051	99.3	3.74	8.59	0.093	19.5	64.7
H0403-8–1	168	764	16	5.05	17.6	36.3	74.6	124	33.8	0.172	256	5.89	7.35	0.678	18.7	33.7
H0405-5	184	670	23.9	7.74	26.2	79	118	56.4	62.2	0.117	165	3.83	11.7	0.959	26	39.8
H0405-6	277	1052	23.5	2.89	18.7	58.2	105	21.8	40.5	0.114	151	4.04	8.17	0.779	32.5	12
H0405-7	480	666	46.7	9.48	17.6	66.4	117	101	52.1	0.51	221	5.74	9.03	0.248	25.9	36.8

Sample number	La	Ce	Pr	Nd	Sm	Eu	Gd	Tb	Dy	Ho	Er	Tm	Yb	Lu	Y	Ta
H0405-10	26.7	53.5	6.62	25.4	6.49	0.329	5.73	1.33	7.85	1.6	4.51	0.882	6.46	0.899	40.3	8.68
H0403-10	36	74.6	9.84	37.6	10.8	0.366	9.56	2.27	13.1	2.67	7.61	1.4	9.73	1.26	72.5	5.03
H0405-8	29.8	58.9	7.63	29	8.59	0.316	8	2.01	12.4	2.51	7.27	1.43	9.58	1.38	75.7	6.55
H0403-8–1	36.6	66.5	8.52	33.8	7.35	1.47	6.67	1.46	7.74	1.49	4.1	0.722	4.55	0.602	40.3	1.58
H0405-5	79	118	17.2	62.2	11.7	2.19	9.75	1.67	8.83	1.52	4.22	0.812	4.27	0.548	39.7	1.75
H0405-6	58.2	105	11.6	40.5	8.17	1.48	6.58	1.06	5.88	1.09	3.09	0.526	3.2	0.436	31	1.61
H0405-7	66.4	117	14.1	52.1	9.03	0.886	8.06	1.43	7.83	1.44	4.31	0.748	4.72	0.655	41	2.89

Exing 1, Exing 2, Exing 3, Exing 4, and Exing 5 based on the Report of 1:20 survey in Ganzhou area (1969)

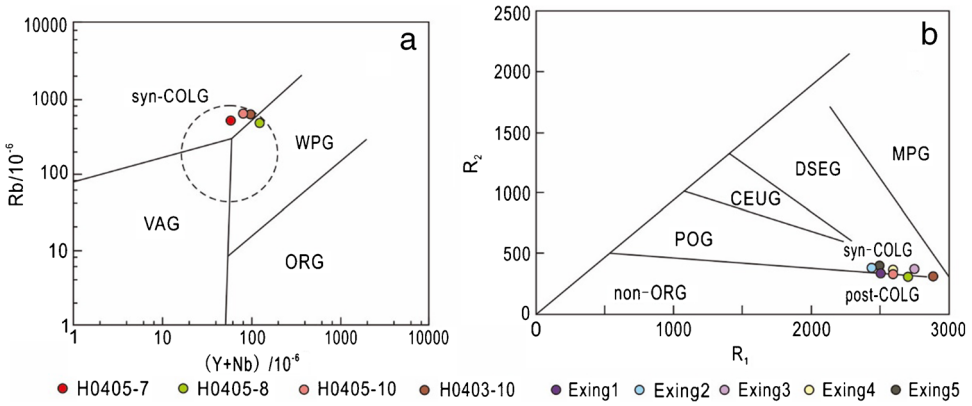

Fig. 11 The diagrams of $(Y+Nb)/10^{-6}$ vs. $Rb/10^{-6}$ (**a**) and R_1 vs. R_2 (**b**) (a, modified after Pearce et al. 1984; b, modified after Batchelor and Bowden (1985)). Data of Early Yanshanian in early stage quoted from Chen et al. (1999), Zhou (2007), Guo et al. (2017), Xue et al. (2011), Li (2019); late stage date quoted from Zhao et al. (2004), Zhou (2007), Deng et al. (2012), Xue et al. (2011), showing the fields of volcanic arc (VAG), ocean-ridge granite (ORG), within-plate granite (WPG), and syn-collisional granite (syn-COLG), mantle plagiogranite (MPG), destructive active slab edge (before plate collision) granite (DSEG), uplift granite after plate collision (CEUG), late-formation granite (POG), non-orogenic A-type granite(non-ORG), post-orogenic A-type granite (post-COLG)

loss, that is, when the water content of the intermediate-acid source rock system is lower, the stable pressure range of plagioclase is larger than that of basic source rocks (Wang 2015, 2016). Therefore, when crystalized mineral assemblage contains plagioclase in equilibrium with high-silicon granite melts, the rocks show low Sr content and obvious negative Eu anomalies. According to the phase diagram, the upper limit of the origin pressure of these granites is 1–1.2 G Pa, which is equivalent to a depth of 35–40 km (Wang 2015).

The zircon Hf isotopic composition of the Guangnan pluton indicates that the source rock of the high-silica granite is the Precambrian crust rock. Zircon U–Pb age dating results show that the biotite granite in the first stage (164 Ma) contains Caledonian and Indosinian residual zircons, the two-mica granite in the second emplacement (159 Ma) contains Caledonian period residual zircon (Table 1, Fig. 4a, c), the biotite granite in the third emplacement (153 Ma) contains a small amount of residual zircon with Early Jurassic age (Table 1), and the fourth stage two-mica granite (148 Ma) contains a small amount of residual zircon from the Indosinian period (Guo Aimin et al., 2017, Table 1). This indicates that the early granitic rocks in the Zhuguangshan area, as part of the source rocks, participated in the formation of the Middle and Late Jurassic high-silica granites, including Caledonian, Indosinian, and Early Jurassic granites.

Field characteristics of the Guangnan pluton showed the lithological change from biotite granite to dimica granite, the intrusion direction changes from southeast to northwest, and the content of dark minerals decreases with the intrusion time. The content of the mafic microgranular enclaves gradually decreases from northwest to southeast in the pluton, the content is high in the Exing area, and the long axis of the mafic microgranular enclaves is distributed in a certain direction with different sizes. The granite from Dongluo area in southwestern also contains a small amount of dark mafic microparticle inclusions (Guo et al. 2017), and they are small. These imply that basic magmatism is one of the heat sources of the crust-derived granitic magma, while magmatic mixing has limited contribution to the material composition of granite formation (Clemens 2012).

Overall, it is deduced that the Guangnan high-silica granite is the product of partial melting of the lower crustal metamorphic pelitic rock and/or metamorphic acidic igneous rock heated by the underplated basic magma in the South China Orogen, and is the product of multiple remelting of the lower crustal materials.

Tectonic significance

Based on previous studies, the Jurassic magmatism in the Nanling area can be divided into two stages, namely, the early Jurassic stage (195–165 Ma) and the late Jurassic stage (165–145 Ma) (Zhou 2007). Some scholars believed that the granite was formed in the background of compression in the late stage of Early Yanshanian (170–150 Ma) in South China (Xu and Tu 1984; Xia and Liang 1991; Chen and Mao 1995; Mao et al. 2008). Others scholars considered that the Late Jurassic granites were mainly formed in the back-arc extensional environment, controlled by the Paleo-Pacific subduction process (Jiang et al. 2015; Liu et al. 2020).

Most discussions on the tectonic background of Jurassic magmatic activity in South China were based on the geochemical characteristics of magmatic rocks. In recent years, some scholars emphasized the methodology and viewpoints of "intrusive rock geotectonics," but magmatic activity is the

only one aspect of the tectonic movement process. "Identifying the tectonic background of magmatic activity should be based on regional geological research, not the geochemical characteristics of granite types or basalts" (Clemens 2003; Wang 2007); the tectonic background of magmatic rocks is the magmatic rock aspect of tectonic research. Therefore, we will discuss the tectonic background of the Guangnan pluton based on the understanding of the Yanshanian tectonic evolution in South China.

Ren (1990) pointed out that the Caledonian orogenic belt in South China is a miogeosyncline fold system, and later evolved into the Post-Caledonian Paraplatform and finally integrated with the Yangtze Paraplatform. The South China was involved into the collided orogenic process between the western Pacific ancient land and the eastern edge of Asia which converted from passive continental margin to active continental margin because of the Indosinian (Akiyoshi) orogenic activity. The Japan-Ryukyu-Taiwan-Palawan zone is a collision orogen between the ancient land of the western Pacific and the eastern part of mainland China. The Yanshanian orogeny stage was the strongest period of the collision activity between the western Pacific ancient land and the eastern edge of Asia (Ren 1990; Ren et al. 1990). Evidence of collision events during the Middle Jurassic (164–161 Ma) from detrital zircons has been found in Hong Kong recent years (Sewell et al. 2016). The Guangnan pluton was formed in 164–148 Ma, and the magma intruded during the early Yanshanian stage based on chronological data. Therefore, tectonically, they should belong to the "syn-collisional" and "post-collisional" granites. On the Y + Nb vs. Rb and the R1 vs. R2 diagram, the Guangnan pluton samples were plotted in the area of the "syn-collisional" and "post-collisional" granites (Fig. 11), which confirmed our understanding based on the tectonic evolution of South China.

As mentioned earlier, the Guangnan pluton has experienced two stages of intrusive activities. In each stage, biotite granites were formed in the earlier, and followed by two-mica granites. Previous studies indicate that large granite bodies in the Nanling area intruded during the Middle and Late Jurassic generally have similar lithological pattern (Wang 2007, Table 1). Therefore, the Guangnan pluton can be used as a representative of the granitic magmatism in the Late Jurassic period in Nanling area. The Nanling area was widely intruded by "syn-collision" to "post-collision" granites during the Middle and Late Jurassic.

Many scholars considered the "post-collision" stage as an extensional structural environment (Shu 2012; Mahdy et al. 2020; Sami et al. 2017). At an extensional regional, the intrusive basic magma is easy to eject out of the surface, together with the acidic magma at the same time, which forms a "bimodal" igneous rock assemblage. A typical example is the bimodal magmatic rock combination developed in the "rift zone" along the east–west direction from western Fujian to southern Jiangxi to southern Hunan intruded during early Jurassic (190–170 Ma) (Chen et al. 1999; He et al. 2010). In the regional compression environment, most of the basic magma is trapped in the lower part of the crust (i.e.: underplating). The heat released from crystallization process of the basic magma provided energy for the lower crustal rocks leading to partial melting, which formed a wide range of acidic magma. During the Middle and Late Jurassic period (170–140 Ma), the Nanling area was characterized by repeated intrusions of large-scale acidic magma, with few basic rocks, and the appearance of magmatic activity was very different from the early Jurassic period (Zhou 2007).

Conclusion

Based on all information acquired and discussed above, combined with previous data, we suggested the following preliminary understanding:

(1) The Guangnan pluton is a compound pluton which formed in the Late Jurassic (164.4–148.2 Ma). The pluton has experienced four batches of magma invasion with 5–6 Myr interval. The magma emplacement can be divided into two stages, and the biotite granite intruded at first, followed by two-mica granite in each stage. First stage is distributed in the Exing area in the northeast of the pluton, and second stage distributed in the Shanggushi-Dongluo in the southwest. The biotite granite is mainly outcropped in the southeastern part of the compound pluton, and gradually transformed into the two-mica granite to northwestern part.

(2) In terms of petrochemistry, the Guangnan pluton is high-silica granite with peraluminum and high potassium and calcium alkalinity characteristics, and shows ferro- and alkali-calcium feature which is similar to the MPG, and the source rocks originated from the Precambrian lower crustal metamorphic pelitic rocks and/or metamorphic intermediate-acid igneous rocks, and the earlier granitic intrusions also provided material source for the Guangnan granite. The heat source for the Guangnan pluton comes from the underplating magma.

(3) The Guangnan pluton was formed in the collisional orogeny stage between the Western Pacific ancient land and the South China orogenic belt during the Middle and Late Jurassic, and was the product of the compression orogeny stage of the Asian continent eastern margin in the early Yanshanian period.

Acknowledgements We sincerely thank Academician Ren Jishun, Institute of Geology, Chinese Academy of Geological Sciences, who fully guided the implementation of this research work, and gave enlightenment and guidance in academic thoughts, which allowed the authors to have a glimpse of the magnificent and beautiful geological landscape in the Nanling area. Xu Tengda and Tian Ye from China University of Geosciences, Beijing, are thanked for their help in the field trips and driver Jiang Dungang for his tirelessly help for several months in the field. This study was financially supported by the China Geological Survey Project (D1912), National Natural Science Foundation of China (40572128, 40376013, 40104003) and the research project of Hebei GEO University on teaching reform (2014J17).

Declarations

Conflict of interest The authors declare no competing interests.

References

Barbarin B (1999) A review of the relationships between granitoid types, their origins and their geodynamic environments. Lithos 46:605–626

Batchelor RA, Bowden P (1985) Petrogenetic interpretation of granitoid rock series using multicationic parameters. Chem Geol 48(1):43–55

Blichertoft J, Albarède F (1997) The Lu-Hf isotope geochemistry of chondrites and the evolution of the mantle-crust system. Earth Planet Sci Lett 148:243–258

Chen YC, Mao JW (1995) Metallogenic series and historical evolution trajectory of mineral deposits in northern Guangxi. Nanning: Guangxi Science and Technology Press, 421–433 (in Chinese with English abstract)

Chen PR, Kong XG, Wang YX, Ni QS, Zhang BT, Ling HF (1999) Rb-Sr isotopic dating and significance of Early Yanshanian bimodal volcanic-intrusive complex from southern Jiangxi province. Geol J China Univ 5(4):378–383 (in Chinese with English abstract)

Chen YC, Wang DH, Xu ZG, Huang F (2014) Outline of regional metallogeny of ore deposits associated with the Mesozoic magmatism in south China. Geotectonica et Metallogenia 38(2):219–229 (in Chinese with English abstract)

Clemens JD (2003) S-type granitic magmas: petrogenetic issues, models and evidence. Earth-Sci Rev 61:1–18

Clemens JD (2012) Granitic magmatism, from source to emplacement: a personal view. Appl Earth Sci 121:107–136

Deng P, Ren JS, Ling HF, Shen WZ, Sun LQ, Zhu B, Tan ZZ (2012) SHRIMP zircon U-Pb ages and tectonic implications for Indosinian granitoids of southern Zhuguangshan granitic composite, South China. Chin Sci Bull 57(14):1231–1241 (in Chinese with English abstract)

Fan FP, Xiao HL, Chen LZ, Cai YT, Li HL (2017) The characteristics of high-differentiation granites and their mineralization in Southern Jiangxi Province-Northern Guangdong Province. Geol Rev 63:171–172 (in Chinese with English abstract)

Frost BR, Barnes CG, Collins WJ, Arculus RJ, Ellis DJ, Frost CD (2001) A geochemical classification for granitic rocks. J Petrol 42:2033–2048

Frost CD, Frost BR, Beard JS (2016) On silica-rich granitoids and their eruptive equivalents. Amer Miner 101:1268–1284

Hunan Geological Survey Institute (2002) Hunan Geological 1: 500,000 Geological and Mineral Map of Nanling Area.

Garcia-Arias M (2020) The never-ending pursuit of a definitive chemical classification system for granites. J Geosci 65:221–227

Griffin WL, Pearson NJ, Belousova E, Jackson SE, van Achterbergh E et al (2000) The isotope composition of cratonic mantle: LAM-MC-ICPMS analysis of zircon megacrysts in kimberlites. Geochim Cosmochim Acta 64:133–147

Guo AM, Chen BH, Chen JF et al (2017) Zircon SHRIMPU-Pb geochronology of granitoids from northern Zhuguangshan granitic composite batholith, Hunan Province. Geol China 44(4):781–792 (in Chinese with English abstract)

He ZY, Xu XS, Niu YL (2010) Petrogenesis and tectonic significance of Mesozoic granite-syenite-gabbro association from inland south China. Lithos 119:621–641

Hou KJ, Li YH, Zou TR, Qu XM, Xie GQ (2009) LA-MC-ICP-MS Zircon Hf isotopes analysis method and geological application. Acta Petrologica Sinica 23:2595–2604 (in Chinese with English abstract)

Jiang Y, Wang G, Liu Z, Ni C, Qing L, Zhang Q (2015) Repeated slab advance-retreat of the Palaeo-Pacific plate underneath SE China. Int Geol Rev 57:472–491

Jiangxi Heavy Industry Bureau (1969) Regional geological and mineral survey report (Ganzhou Sheet) (volume I):38–72. (in Chinese)

Li XH (1990) The age of magmatic activity and crustal movement of the Wanyangshan-Zhuguangshan batholith. Sci China B 20(7):747–755 (in Chinese with English abstract)

Li W (2019) Zircon U-Pb dating of the Yingqian granodiorite of the South Jiangxi and its relations to mineralization. Yangtze University, 25–61 (in Chinese with English abstract)

Liu YS, Gao S, Hu ZC, Gao CG, Zong KQ, Wang DB (2010) Continental and oceanic crust recycling-induced melt-peridotite interactions in the Trans-North China Orogen: U-Pb dating, Hf isotopes and trace elements in zircons from mantle xenoliths. J Petrol 51:537–571

Liu JX, Wang S, Wang XL, Dua DH, Xing GF, Fu JM, Chen X, Sun ZM (2020) Refining the spatio-temporal distributions of Mesozoic granitoids and volcanic rocks in SE China. J Asian Earth Sci 201:104503

Lu YJ, Loucks RR, Fiorentini ML, Yang ZM, Hou ZQ (2015) Fluid flux melting generated postcollisional high Sr/Y copper ore–forming water-rich magmas in Tibet. Geology 43(7):583–586

Mahdy NM, Ntaflos T, Pease V, Sami M, Slobodník M, Abu Steet A, Abdelfadil KM, Fathy D (2020) Combined zircon U-Pb dating and chemical Th-U-total Pb chronology of monazite and thorite, Abu Diab A-type granite, Centtral Eastern Desert of Egypt: constrains on the timing and magmatic-hydrothermal evolution of rare metal ganitic magmatism in Arabian Nubian Shield. Geochemistry 80(4):125669

Maniar PD, Piccolli PM (1989) Tectonic discrimination of granitoids. Geol Soc Am Bull 101(5):635–643

Mao JR, Gao QH, Li ZL, Zhong DL, Ye HM, Zhao XL, Zhou J, Hu Q, Zeng QT (2008) Correlation of Mesozoic-Cenozoic tectono-magmatism between SE China and Japan. Geol Bull China 287:28–40 (in Chinese with English abstract)

Mao JW, Xie GQ, Cheng YB, Chen YC (2009) Mineral deposit models of Mesozoic ore deposits in South China. Geol Rev 55(3):347–354 (in Chinese with English abstract)

Middlemost EAK (1994) Naming materials in the magma/igneous rock system. Earth-Sci Rev 37(3–4):215–224

Miller CF, Miller JS, Gualda GAR (2020) Felsic magma diversity & triumphs and perils of granite typology. Goldschmidt 2020 Conference Abstracts:1804

Naney MT (1983) Phase equilibria of rock-forming ferromagnesian silicates in granitic systems. Am J Sci 283:993–1033

Pearce JA, Harris NBW, Tindle AG (1984) Trace element discrimination diagrams for the tectonic interpretation of granitic rocks. J Petrol 25(4):956–983

Ren JS, Niu BG, Wang J, He ZJ, Jin XC, Xie LZ, Zhao L, Liu RY, Jiang XJ, Li S, Yang FL (2013) 1:5 million international geological map of Asia. Acta Geosci Sin 34(1):24–31 (in Chinese with English abstract)

Ren JS, Chen TY, Niu BG, Liu ZG, Liu FR (1990) Tectonic evolution of the continental lithosphere and metallogenesis in eastern China and adjacent areas. Beijing: Science Press, 1–194 (in Chinese with English abstract)

Ren JS (1990) On the geotectonics of Southern China. Acta Geol Sin 64(4):275–288 (in Chinese with English abstract)

Ren JS, Li C (2016) Cathaysia old land and relevant problems: Pre-Devonian tectonics of Southern China. Acta Geol Sin 90(4):607–614 (in Chinese with English abstract)

Sami M, Ntaflos T, Farahat ES, Mohamed HA, Ahmed AF, Hauzenberger C (2017) Mineralogical, geochemical and Sr-Nd isotopes characteristics of fluorite-bearing granites in the Northern Arabian-Nubian Shield, Egypt: constraints on petrogenesis and evolution of their associated rare metal mineralization. Ore Geol Rev 88:1–22

Sewell RJ, Carter A, Rittner M (2016) Middle Jurassic collision of an exotic microcontinental fragment: Implications for magmatism across the Southeast China continental margin. Gondwana Res 38:304–312

Shu LS (2012) An analysis of principal features of tectonic evolution in South China Block. Geol Bull China 32(7):1035–1053 (in Chinese with English abstract)

Shu LS, Zhou XM, Deng P, Wang B, Jiang SY, Yu JH, Zhao XX (2009) Mesozoic tectonic evolution of the southeast China Block: new insights from basin analysis. J Asian Earth Sci 34:376–439

Shu L S, Yao J L, Wang B, Faure M, Charvet J, Chen Y (2021) Neoproterozoic plate tectonic process and Phanerozoic geodynamic evolution of the South China Block. Earth-Sci Rev 103596. https://doi.org/10.1016/j.eatscirev.2021.103596

Soderlund U, Patchett PJ, Vervoort JD, Isachsen CE (2004) The ^{176}Lu decay constant determined by Lu-Hf and U-Pb isotope systematics of Precambrian mafic intrusions. Earth Planet Sci Lett 219:311–324

Sun LQ (2018) Petrogenesis of the Mesozoic granites in the Zhuguangshan area in the Nanling region and their implications for the uranium Mineralization. Nanjing University, 98–144 (in Chinese with English abstract)

Sun SS, McDonough WF (1989) Chemical and isotopic systematics of oceanic basalts: implications for mantle composition and processes. Geol Soc Lond Spec Publ 42:313–345

Tong LH, Wang Y (2013) Ferroan granitoids: definition, classification and origination. Bull Mineral Petrol Geochem 31(3):370–378 (in Chinese with English abstract)

Wang Y (2007) A discussion on some problems in the research on the Mesozoic potassic igneous rocks in Eastern China. Geol Rev 53(2):198–206 (in Chinese with English abstract)

Wang Y (2008a) Some further discussions on the genetic type of the Early Yanshanian (Jurassic) granitoids in the Nanling area, SE China. Geol Rev 54(2):162–174 (in Chinese with English abstract)

Wang Y (2008b) Petrogenesis of the Jurassic aluminous A-type granite in the Nanling area South China and its constration on paleo-geotherm. Geotectonica et Metallogenia 32(3):365–381 (in Chinese with English abstract))

Wang Y (2015) Does "Guangxi-type granite" have petrological significance? ——A critique on "Geochemistry of Guangxi-type granite and its tectonic implications". Acta Petrologica et Mineralogica 34(3):427–439 (in Chinese with English abstract)

Wang Y (2016) A discussion on some basic conceptions and problems related to the experimental study of adakite. Acta Petrologica et Mineralogica 35(1):162–176 (in Chinese with English abstract)

Wang Y, Jiao YL, Tong LH, Yao Y (2013) The essence of A-type granitoids: a discussion on the opinions held by Prof. Zhang Qi and some other researchers. Acta Petrologica et Mineralogica 32(2):260–266 (in Chinese with English abstract)

Xia HY, Liang SY (1991) Genesis series of W-Sn rare metal granite deposits in South China. Beijing: Science Press, 61–182 (in Chinese with English abstract)

Xia JL, Huang GC, Ding L, Ding LX, Chen XQ, Ji WB (2021) Chronological framework of the Zhuguangshan composite batholith in the Nanling Area. South China Geol 37(3):280–297 (in Chinese with English abstract)

Xing GF, Lu QD, Chen R, Zhang ZY, Nie TC, Li LM, Huang JL (2008) Study on the ending time of Late Mesozoic tectonic regime transition in South China——comparing to the Yanshan area in North China. Acta Geol Sin 82(4):451–463 (in Chinese with English abstract)

Xu KQ, Tu GC (1984) Geology of granites and their metallogenetic relation. Science Press, Beijing (in Chinese with English abstract)

Xue P, Zhang SG, Yuan Y, Han SL, Yao CX (2011) Mineralization characters and prospecting marks of Neidong W-Mo polymetallic deposit in north Guangdong. Southern Metal, (4):22–26+30 (in Chinese with English abstract)

Zhao L, Yu JH, Xie L (2004) Geochemistry and origin of the Hongshan topaz-bearing leucogranites in southwestern Fujian Province. Geochimica 33(4):372–386 (in Chinese with English abstract)

Zheng JJ (1988) The stage division of Zhuguangshan compound pluton. China Reg Geol 15(4):32–37 (in Chinese with English abstract)

Zhou XM (2007) Genesis and lithospheric dynamic evolution of Late Mesozoic granites in Nanling area. Beijing: Science Press, 3–683 (in Chinese with English abstract)

Zhou XM, Sun T, Shen WZ, Shu LS, Niu YL (2006) Petrogenesis of Mesozoic granitoids and volcanic rocks in South China: a response to tectonic evolution. Episodes 29(1):26–33